

**The DEEP Groth Strip Survey XII: The Metallicity of Field Galaxies at  
 $0.26 < z < 0.82$  and the Evolution of the Luminosity-Metallicity Relation**

Henry A. Kobulnicky

*Department of Physics & Astronomy  
University of Wyoming  
Laramie, WY 82071  
Electronic Mail: chipk@uwoyo.edu*

Christopher N. A. Willmer<sup>1</sup>, Benjamin J. Weiner,  
David C. Koo, Andrew C. Phillips, & S. M. Faber

*University of California, Santa Cruz  
Department of Astronomy & Astrophysics  
Santa Cruz, CA, 95064*

*cnaw@ucolick.org, bjw@ucolick.org, koo@ucolick.org, phillips@ucolick.org, faber@ucolick.org*

Vicki L. Sarajedini

*Department of Astronomy  
University of Florida  
Gainesville, FL 32611  
vicki@astro.ufl.edu*

Luc Simard

*Canadian Astronomy Data Centre  
Herzberg Institute of Astrophysics  
National Research Council of Canada  
luc.simard@nrc.ca*

Nicole P. Vogt

*Department of Astronomy  
New Mexico State University  
P.O. Box 30001, Dept 4500  
Las Cruces, NM 88003-8001  
nicole@nmsu.edu*

Revised draft of 28 April 2003

**ABSTRACT**

Using spectroscopic data from the Deep Extragalactic Evolutionary Probe (DEEP) Groth Strip survey (DGSS), we analyze the gas-phase oxygen abundances for 56 emission-line field galaxies in the redshift range  $0.26 < z < 0.82$ . These galaxies comprise a small subset selected from among 693 objects in the DGSS. They are chosen for chemical analysis because they exhibit the strongest emission lines, and thus have the highest star formation rates per unit luminosity. Oxygen abundances relative to hydrogen range between  $8.4 < 12 + \log(O/H) < 9.0$  with typical uncertainties of 0.17 dex. The 56 DGSS galaxies collectively exhibit a correlation between B-band luminosity and metallicity, i.e., an L-Z relation. Using the DGSS sample and local galaxy samples for comparison, we searched for a “second parameter” which might explain some of the dispersion in the L-Z relation. Parameters such as galaxy color, emission line equivalent width, and effective radius were explored but found to be uncorrelated with residuals from the the mean L-Z relation. The source of the dispersion in the L-Z relation is either intrinsic or depends upon a yet-unidentified combination of parameters.

Subsets of DGSS galaxies binned by redshift also exhibit L-Z correlations but with different zero points. Galaxies in the highest redshift bin ( $z = 0.6 - 0.82$ ) are brighter by  $\sim 1$  mag compared to the lowest redshift bin ( $z = 0.26 - 0.40$ ) and brighter by  $\sim 1 - 2$  mag compared to local ( $z < 0.1$ ) field galaxies. This offset from the local L-Z relation is greatest for objects at the low-luminosity ( $M_B \sim -19$ ) end of the sample, and vanishingly small for objects at the high-luminosity end of the sample ( $M_B \sim -22$ ). Thus, both the slope and zero point of the L-Z relation appear to evolve. Based on the DGSS galaxies, we provide an approximate analytic expression for the mean gas-phase metallicity of galaxies as a function of luminosity and redshift—a recipe that may aid in modeling the properties of cosmologically distant galaxies. Emission-line field galaxies have undergone moderate amounts of evolution in the past  $\sim 7$  Gyr since  $z \sim 0.8$ , and the evolution is most significant for galaxies of lower luminosity. Either the least-luminous DGSS field galaxies have faded by 1–2 mag due to decreasing levels of star formation, or they have experienced an increase in the mean metallicity of the interstellar medium by factors of 1.3–2 (0.1–0.3 dex). Plausible evolutionary models suggest that a combination of the two processes is likely. The relatively greater degree of luminosity and metallicity evolution seen among the lower luminosity (sub  $L^*$ ) galaxies in the last 8 Gyr implies either a more protracted assembly process, or a more recent formation epoch compared to more luminous  $L^*$  galaxies.

*Subject headings:* ISM: abundances — ISM: H II regions — galaxies: abundances — galaxies: fundamental parameters — galaxies: evolution — galaxies: starburst

---

<sup>1</sup>On leave from Observatório Nacional, Rio de Janeiro, Brazil

## 1. Metallicity as a Measure of Galaxy Evolution

Many recent research programs in galaxy evolution trace changes in correlations between fundamental galaxy properties as a function of cosmic epoch. One such approach compares the number density and luminosity function of galaxies at earlier times (Lilly *et al.* 1995; Bershady *et al.* 1997; Sawicki, Lin, & Yee 1997; Lin *et al.* 1999; ) to the luminosity function in the nearby universe (Zucca *et al.* 1997; Marzke *et al.* 1998; Norberg *et al.* 2002). Evidence suggests an increase in the number density of small, blue galaxies at earlier times with only a small amount of passive fading among the more luminous, redder galaxies. Other investigations compare the relation between rotation velocity and luminosity (T-F relation; Tully & Fisher 1977) locally with that observed in more distant disk galaxies (e.g., Forbes *et al.* 1995; Vogt *et al.* 1996, 1997; Simard & Pritchett 1998). Most results indicate that galaxies of a given rotational amplitude appear 0.2-1.0 mag brighter at  $z \sim 1$ , although Bershady *et al.* (1998) argue that the variation is significant for only the bluest galaxies, and Kannappan, Fabricant & Franx (2002) show that Tully-Fisher residuals are strongly correlated with galaxy color. Simard *et al.* (1999) find no evidence for evolution of the size-magnitude relation among 190 field galaxies out to  $z = 1.1$  in the Groth Strip (Groth 1994). They show that selection effects favor high surface brightness galaxies in existing surveys. These biases may mimic the appearance of luminosity evolution and/or surface brightness evolution reported in many studies (Schade *et al.* 1996a, 1996b; Roche *et al.* 1998; Lilly *et al.* 1998). Yet another line of investigation compares the fundamental plane<sup>2</sup> correlations for early-type galaxies as a function of epoch. Recent results suggest an decrease in the mean mass-to-light ratio with lookback time for elliptical galaxies (van Dokkum & Franx 1996; Kelson *et al.* 1997). In Paper X of this series, Im *et al.* (2001) found a brightening of 1-2 mag for early-type  $L^*$  galaxies out to  $z \sim 1$ .

In this paper we focus on the evolution of the correlation between metallicity,  $Z$ , and total luminosity, i.e., the luminosity-metallicity (L-Z) relation to which nearly all types of *local* galaxies conform. In early-type systems, absorption line indices provide a measure of the mean stellar iron or magnesium abundances (Faber 1973; Brodie & Huchra 1991; Trager 1999) while in spiral (Zaritsky, Kennicutt, & Huchra 1994) and dwarf systems (Lequeux *et al.* 1979; French 1980; Skillman, Kennicutt, & Hodge 1989; Richer & McCall 1995) the H II region oxygen abundance relative to hydrogen is the basis of metallicity measurement. The luminosity-metallicity relation (L-Z) can be used as a sensitive probe and consistency check of galaxy evolution. The metallicity of a galaxy can only increase monotonically with time (unless large-scale infall of primordial gas is invoked), while the luminosity may increase or decrease depending on the instantaneous star formation rate. Metallicity is less sensitive to variations due to transient star formation events in a galaxy’s history. Most models and observations of galaxies at earlier epochs predict higher star formation rates and a larger fraction of blue, star-forming galaxies in the past (Madau *et al.* 1996;

---

<sup>2</sup>The fundamental plane is the locus populated by early type galaxies in the three-dimensional parameter space of surface brightness, velocity dispersion, and size (parameterized by effective radius) (Dressler *et al.* 1987; Djorgovski & Davis 1987).

Lilly *et al.* 1996; Somerville & Primack 1999). Thus, a high or intermediate-redshift galaxy sample ought to be systematically displaced from the local sample in the luminosity-metallicity plane if individual galaxies participate in these cosmic evolution processes. However, if local effects such as the gravitational potential and “feedback” from winds and supernovae regulate the star formation and chemical enrichment process, then the L-Z relation might be independent of cosmic epoch. Semi-analytic models of Somerville & Primack (1999), for example, show very little evolution of the L-Z relation with redshift. One goal of this paper is to provide data capable of testing these alternative hypotheses.

At high redshift, absorption line surveys have been tracing the chemical evolution of the Lyman-alpha forest and damped Lyman-alpha systems for more than a decade (Bergeron & Stasińska 1986; Sargent *et al.* 1988; Steidel 1990; Pettini *et al.* 1997; Lu, Sargent, & Barlow 1997; Prochaska & Wolf 1999), while several studies have recently begun to trace the cosmic chemical evolution of *individual galaxies* with known morphological and photometric properties. Kobulnicky & Zaritsky (1999) measured H II region oxygen and nitrogen abundances for a sample of 14 compact starforming galaxies with kinematically narrow emission lines in the range  $z = 0.1 - 0.5$ . Their sample was found to conform to the local L-Z relation, within observational uncertainties. Carollo & Lilly (2001) studied 13 star-forming galaxies at  $0.5 < z < 1$  from the Canada-France Redshift Survey (CFRS; Lilly *et al.* 1995) and found no significant evidence for evolution in the L-Z relationship out to  $z=1$ . However, at larger redshifts of  $z > 2$ , both Kobulnicky & Koo (2000) and Pettini *et al.* (2001) found that Lyman break galaxies with metallicities between  $0.1 Z_{\odot} < Z < 0.8 Z_{\odot}$  are 2-4 magnitudes more luminous than local galaxies of similar metallicity. This deviation from the local L-Z relation demonstrates that the luminosity-to-metal ratio varies throughout a galaxy’s lifetime and is a potentially powerful diagnostic of its evolutionary state.

The DEEP (Deep Extragalactic Evolutionary Probe; Vogt *et al.* 2003; Paper I) team has been assembling Keck spectroscopic data on galaxies in the Groth Strip survey (Groth 1994) in order to study the evolution of field galaxies. Previous papers in this series include a study of the evolution of the Fundamental Plane (FP) of early-type galaxies (Paper IX; Gebhardt *et al.* 2003), the evolution of the luminosity function of E/S0 galaxies (Paper X; Im *et al.* 2001), and the structural parameters of Groth Strip galaxies (Simard *et al.* 2002; Paper II). In this paper, we explore the chemical properties of 56 star-forming emission-line field galaxies observed as part of the DEEP Groth Strip Survey (DGSS). We measure the interstellar medium oxygen abundances from the [O II], [O III], and  $H\beta$  emission lines to analyze the degree of metal enrichment as a function of redshift, luminosity, and other fundamental parameters. Throughout, we adopt a cosmology with  $H_0=70 \text{ km s}^{-1} \text{ Mpc}^{-1}$ ,  $\Omega_m = 0.3$ , and  $\Omega_{\Lambda} = 0.7$ .

### 1.1. Target Selection and Observations

The DEEP Groth Strip Survey (DGSS) consists of Keck spectroscopy over the wavelength range  $\sim 4400 \text{ \AA} - 9500 \text{ \AA}$  obtained with the Low Resolution Imaging Spectrometer (LRIS; Oke

*et al.* 1995). The spectra have typical resolutions of 3-4 Å. Integration times ranged from 3000 s to 18,000 s with a mean of around 6000 s. A full description appears in Vogt *et al.* (Paper I in this series; 2003).

We searched the spectroscopic database for galaxies in the Groth Strip Survey with nebular emission lines suitable for chemical analysis. Only galaxies where it was possible to measure all of the requisite [O II]λ3727, Hβ, [O III]λ4959, and [O III]λ5007 lines were retained. These criteria necessarily exclude objects at redshifts of  $z \lesssim 0.26$  since the requisite [O II]λ3727 line falls below the blue limit of the spectroscopic setup. Likewise, objects with redshifts  $z \gtrsim 0.82$  are excluded because the [O III]λ5007 line falls beyond the red wavelength limit of the survey. As of February 2002, there were 693 objects with Keck spectra with identified redshifts in the DEEP Groth Strip Survey. Of these 693 objects, 398 unique objects have spectroscopic redshifts between within the nominal limits  $0.26 < z < 0.82$ . The usable sample is further reduced because 23 candidates were positioned on the slitmask such that the [O III] lines fell off the red end of the spectral coverage. An additional 49 objects were rejected because their position on the slitmask caused the [O II]λ3727 line to fall off the blue end of the spectral coverage. Furthermore, atmospheric O<sub>2</sub> absorption troughs between 6865 Å – 6920 Å (the “B band”) and between 7585 Å – ~ 7680 Å (the “A band”) prohibit accurate measurement of emission lines for objects in particular redshifts ranges. We removed 14 objects from the sample in the redshift interval  $0.410 < z < 0.426$  where the Hβ line falls in the B band. We removed 8 additional objects in the redshift interval  $0.56 < z < 0.58$  where Hβ falls in the A band. We removed 24 objects in the redshift interval  $0.52 < z < 0.54$  which places both [O III] λ4959 and [O III] λ5007 in the A band. The B band is sufficiently narrow that either [O III] λ4959 or [O III] λ5007 is always available for measurement. Following this selection process, 276 objects remain.

A further list of 210 objects were removed from the sample because the Hβ emission line was absent or too weak (S/N<8:1) for reliable chemical determinations (Kobulnicky, Kennicutt, & Pizagno 1999 for a discussion of errors and uncertainties). The spectra of objects rejected due to a weak Hβ line are usually dominated by stellar continuum rather than nebular emission from star-forming regions. Most local early-type spirals and elliptical galaxies share these spectral characteristics. For these objects, Hβ is seen in absorption against the stellar spectrum of the galaxy. Thus early type galaxies with older stellar populations are preferentially rejected in favor of late type galaxies with larger star formation rates. There should, however, be no metallicity bias introduced by rejecting these 210 objects since we will compare the DGSS sample with a local sample selected in the same manner: on the basis of emission lines measured with a signal-to-noise of 8:1 or better.

Objects with strong Hβ but immeasurably weak [O II] or [O III] lines present a data selection conundrum. In principle, such objects should be included in the sample to avoid introducing a metallicity bias, but it is not possible to compute metallicities if the oxygen lines are not detected. Only 3 such objects were found in the database. For these objects, it appears that poor sky subtraction caused the [O III] features to be immeasurably weak. Intrinsically-weak oxygen lines

may be caused by either extremely high ( $Z > 2 Z_{\odot}$ ) or extremely low ( $Z < 0.05 Z_{\odot}$ ) metal content. In the latter case, oxygen lines are weak because of the lack of  $O^+$  and  $O^{++}$  ions. However, in the local universe, galaxies with extremely low intrinsic abundances are under-luminous ( $M_B > -15$ ), and no such faint galaxies are included in our sample. In the high-metallicity case, efficient cooling decreases the mean collisional excitation level, reducing the [O III] line strengths. However, the Balmer lines and [O II] lines are not strongly affected by reductions in electron temperature. It is unlikely that our rejection criteria bias the sample by preferentially excluding either metal-poor or metal-rich systems.

Of the original 693 objects, 66 galaxies remain. These objects appear in Table 1, along with their equatorial coordinates, redshift, absolute blue magnitude, restframe  $(B - V)_0$  color, half-light radius  $R_{hl}$ , and bulge fraction  $B/T$  derived from model fitting routines (Simard *et al.* 1999, 2002). The restframe  $(B - -V)_0$  and  $(B - -R)_0$  colors used in this work were calculated following the procedure of Lilly *et al.* (1995), by interpolating the measured colors of DGSS galaxies over a subset of Kinney *et al.* (1996) spectra, which were then used to synthesize the different restframe colors. Figure 1 shows their redshifted spectra with major emission lines identified next to the F814W HST greyscale images. A cursory glance at the images reveals an assortment of galaxy types, from small compact objects to spiral disks and obvious mergers-in-progress.

In order to assess whether the 66 selected objects are representative of the 398 galaxies with spectra in the  $0.25 < 0.82$  redshift range, Figure 2 shows histograms of their morphological and photometric properties. The six panels show the redshift distribution  $z$ , the absolute B magnitude  $M_B$ , the rest-frame color  $(B - V)_0$ , the half-light radius  $R_{hl}$ , the bulge fraction  $B/T$ , and the total asymmetry index,  $R_T + R_A^3$ . Examination of Figure 2 reveals that the 66 galaxies selected for chemical analysis are representative of the entire DEEP sample in terms of their luminosities, redshift distributions, sizes, and bulge fractions, but they are preferentially bluer and more asymmetric than the sample as a whole. This disproportionate fraction of asymmetric galaxies with strong emission lines may be understood either 1) as mergers which trigger star formation and produce H II regions, or 2) isolated galaxies dominated by star-forming regions which give rise to an asymmetric morphology. The possible systematic effects introduced by the selection criteria will be discussed further below.

## 2. Spectral Analysis

### 2.1. Emission Line Measurements

Spectra taken on different observing runs with different slitmasks enable us to combine multiple spectra for most DGSS galaxies. After wavelength calibrating each spectrum, we combined the

---

<sup>3</sup>Definitions of DGSS structural parameters may be found in Paper II of this series, Simard *et al.* (2002).

available 2-dimensional spectra to produce a master spectrum with higher signal-to-noise. We then extracted an optimal 1-D spectrum for analysis. The spectra are not flux calibrated. We manually measured equivalent widths of the emission lines present in each spectrum with the IRAF SPLIT routine using Gaussian fits. The [O II] doublet, which is visibly resolved, was fit with two Gaussian components and the sum recorded. Table 1 lists the equivalent widths and measurement uncertainties for each line. Where [O III]  $\lambda$ 4959 was below our nominal S/N threshold of 8:1, we calculated the EW based on the strength of [O III]  $\lambda$ 5007 assuming an intrinsic ratio of 3:1. The reported equivalent widths are corrected to the rest frame using

$$EW_{rest} = EW_{observed}/(1 + z) \quad (1)$$

Associated uncertainties are computed taking into account both the uncertainty on the line strength and the continuum level placement using

$$\sigma_{EW} = \sqrt{\frac{1}{C^2}\sigma_L^2 + \frac{L^2}{C^4}\sigma_C^2}, \quad (2)$$

where  $L$ ,  $C$ ,  $\sigma_L$ , and  $\sigma_C$  are the line and continuum levels in photons and their associated  $1 \sigma$  uncertainties. We determine  $\sigma_C$  manually by fitting the baseline regions surrounding each emission line multiple times. We adopt  $\sigma_L = \sqrt{12} \times RMS$  where 12 is the number of pixels summed in a given emission line for this resolution, and RMS is the root-mean-squared variations in an adjacent offline region of the spectrum. Using this empirical approach, the stated uncertainties implicitly include errors due to Poisson noise, sky background, sky subtraction, readnoise, and flatfielding. In nearly all cases, the continuum can be fit along a substantial baseline region, so that  $\sigma_C \ll \sigma_L$ .

## 2.2. AGN Contamination

In the analysis that follows, accurate assessment of the chemical abundances in the warm ionized medium requires that the observed emission lines arise in H II regions powered by photoionization from massive stars. Non-thermal sources such as active galactic nuclei (AGN) often produce emission-line spectra that superficially resemble those of star-forming regions. AGN must be identified as such because blindly applying emission-line metallicity diagnostics calibrated from H II region photoionization models will produce erroneous metallicities.

Traditionally, AGN can be distinguished from starbursts on the basis of distinctive [N II]/H $\alpha$ , [S II]/H $\alpha$ , [O I]/H $\alpha$ , and [O II]/[O III] line ratios (see Heckman 1980; Baldwin, Phillips, & Terlevich 1981; Veilleux & Osterbrock 1987). However, some or most of these diagnostic lines are unobservable in the current generation of ground-based optical surveys at increasingly higher redshifts. Sometimes, as in this survey, only equivalent width measurements are available. With these limitations in mind, Rola, Terlevich, & Terlevich (1997) have explored using ratios of  $EW_{[O II]}$  and

$EW_{H\beta}$  as substitute diagnostics for identifying AGN.

Figure 3 shows diagnostic diagrams,  $EW_{[O II]}/EW_{H\beta}$  and  $EW_{[O III]}/EW_{H\beta}$  versus  $\log EW_{H\beta}$ , for the identification of AGN and starforming galaxies based on Rola *et al.* (1997). The upper panels of Figure 3 plot  $EW_{[O III]}/EW_{H\beta}$ . Filled symbols denote the DGSS objects. For a comparable sample of local star-forming galaxies, we compiled three sets of spatially-integrated (i.e., global) emission-line spectra from the literature. The first set, consisting of 22 objects, comes from the 55-object spectroscopic galaxy atlas of Kennicutt (1992b). For each galaxy with detectable (S/N>8:1) [O II] $\lambda$ 3727, [O III] $\lambda$ 4959, [O III] $\lambda$ 5007, and H $\beta$  emission, we measured the emission-line fluxes and equivalent widths. Dereddened emission-line fluxes were computed by comparing the observed  $F_{H\alpha}/F_{H\beta}$  ratios to theoretical ratios ( $I_{H\alpha}/I_{H\beta} = 2.75$ - $2.85$  for wide temperature range; here we assume a fixed electron temperature of 12,000 K)<sup>4</sup>. As a second local sample, we selected the compilation of nearby field galaxies from Jansen *et al.* (2000a,b; NFGS), adopting their published emission-line fluxes and equivalent widths. The Nearby Field Galaxy Survey is a collection of 200 local ( $z < 0.04$ ) morphologically diverse galaxies selected from the CfA I redshift catalog (Huchra 1983) which has the virtue of being nearly complete to the photographic limits of the survey. See Jansen *et al.* (2000a) for a discussion of the differences between the NFGS and K92 samples. Briefly, the K92 objects have a higher fraction of star-forming galaxies (objects with strong emission lines) compared to the NFGS sample. As a third local sample, we chose the emission-line selected galaxies from the Kitt Peak National Observatory Spectroscopic Survey (KISS; Salzer *et al.* 2000). KISS is a large-area objective prism survey of local ( $z < 0.09$ ) galaxies selected by strong H $\alpha$  emission lines.

In Figure 3, the distribution of DGSS objects is similar to the distribution of KISS and K92 objects in having relatively large  $EW_{H\beta}$  and high  $EW_{[O III]}/EW_{H\beta}$  ratios. In comparison, the NFGS galaxies have lower mean  $EW_{H\beta}$ . Open symbols show a comparison sample of K92 local galaxies. Skeletal triangles denote the NFGS galaxies. Dots indicate the KISS galaxies. Filled symbols coded by redshift interval denote the new DGSS objects presented here. In the left panels we plot the raw equivalent width data, while in the right panels we add 3 Å to the  $EW_{H\beta}$  as a rough correction for underlying Balmer absorption in the stellar population. Solid lines indicate the regions described by Rola *et al.* as likely to contain AGN. AGN typically occupy the upper left and upper right sectors while starforming H II galaxies typically fall in the lower right and lower left regions. Many of the normal starforming local galaxies from the K92 and NFGS compilations also lie in parameter space ostensibly occupied by AGN, even in the right panels where we have applied the 3Å correction for absorption. It seems that, on the basis of equivalent width ratios, there is considerable ambiguity regarding object classification. We have chosen to be conservative and remove from our sample the 8 objects which fall in this region of the diagram given by  $EW_{[O II]}/(EW_{H\beta}) > 5$  (dashed line) in the left (absorption uncorrected) panels. These 8 objects

---

<sup>4</sup>Direct measurements of the electron temperature are not possible from these data since the temperature-sensitive [O III]  $\lambda$ 4363 line is not detected and the upper limits do not provide useful constraints.



are colored magenta in Figure 3. Even if some fraction of these 8 objects are falsely flagged as AGN, their exclusion from the larger sample will not have a significant impact on the conclusions drawn from the 56 remaining galaxies.

From examination of the spectra in Figure 1, we selected two additional objects as probable AGN based on their anomalously large ratios of [Ne III]  $\lambda 3868$  to [O II]  $\lambda 3727$ . Objects 092-7832 and 203-3109 do not stand out in Figure 3, but have  $EW_{[Ne\ III]\lambda 3826}/EW_{[O\ II]\lambda 3727} > 0.4$ , compared to  $EW_{[Ne\ III]\lambda 3826}/EW_{[O\ II]\lambda 3727} \sim 0.1 - 0.2$  for normal starforming objects in K92 Osterbrock (1989) notes the presence of enhanced [Ne III] as a common signature in AGN and LLINERs. Another paper in this series will contain a more complete discussion of the AGN population in the DGSS (Sarajedini *et al.* 2003; Paper XIII).

Nine of the lowest redshift objects have measurable  $H\alpha$  and [N II] emission lines which can be used to place them on the more traditional AGN diagnostic diagrams (e.g., Baldwin, Phillips, & Terlevich 1981; Veilleux & Osterbrock 1987). All of these objects have [N II]/ $H\alpha$  and [O III] line ratios consistent with normal star-forming galaxies, [N II]/ $H\alpha \simeq 0.1$ . These 9 objects would have already been classified as star-forming galaxies on the basis of our provisional [O II]/ $H\beta$  diagnostic in Figure 3. Unfortunately, none of the possible AGN identified above can be checked in this manner because the  $H\alpha$  and [N II]  $\lambda 6584$  lines are not included in the spectral coverage.

In summary, 10 objects have been identified as possible AGN and removed from the sample of 66 galaxies, leaving 56 intermediate-redshift field galaxies for further analysis. Blindly including the 10 probable AGN in the sample would reduce the mean metallicity of DGSS galaxies (i.e., probable AGN preferentially scatter to the metal-poor or overly-luminous side of the L-Z relation).

Figure 4 shows in greater detail the distribution of magnitude, color, restframe  $EW_{H\beta}$  and  $H\beta$  luminosity for the 56 remaining galaxies compared to the original set of 276 DGSS objects with emission lines in the range  $0.26 < z < 0.82$ . Symbols distinguish objects by redshift: “low” (14 objects;  $0.26 < z < 0.40$ ), “intermediate” (19 objects;  $0.40 < z < 0.60$ ), and “high” (24 objects;  $0.60 < z < 0.82$ ). Filled symbols denote galaxies selected for chemical analysis, while open symbols denote the entire set of galaxies in each redshift interval. Points with error bars denote the means and dispersions of each sample. The lower row shows  $(B - V)_0$  color versus  $M_B$ . Objects in the lowest redshift bin exhibit a remarkable correlation between luminosity and  $(B - V)_0$  color, while the samples in the latter two redshift bins do not. The two highest redshift bins contain a higher fraction of luminous blue objects which are absent in the low-redshift bin. In the high-redshift bin, the magnitude-limited nature of the sample becomes obvious, as there are no galaxies fainter than  $M_B = -18$ . In all redshift bins, the selected galaxies are preferentially those with the highest  $EW_{H\beta}$  and the bluest colors. This effect is most significant in the highest redshift bin. The correlation between blue magnitude and  $H\beta$  luminosity in all three redshift bins merely reflects the fact that the  $H\beta$  luminosities were computed from  $M_B$  and  $EW_{H\beta}$ . No extinction correction has been applied. Put simply, more luminous objects are capable of sustaining greater rates of star formation. The distribution of equivalent widths indicates that the star formation per unit

luminosity is roughly similar for galaxies in the two highest redshift intervals, but that the lowest redshift bin has fewer objects with large EW. This is most likely a volume effect since there will be fewer extreme starburst objects in the smaller volume at  $0.26 < z < 0.40$ .

### 3. Analysis

#### 3.1. Assessing the Physical and Chemical Properties of the Sample

Oxygen is the most easily measured metal in H II regions due to its strong emission lines from multiple ionization species in the optical portion of the spectrum. Measurement of the oxygen abundance relative to hydrogen is based upon the intensity ratio of the collisionally excited [O II] $\lambda$ 3727 and [O III] $\lambda$ 4959,5007 lines relative to Balmer series recombination lines (e.g., H $\beta$ ) using the standard analysis techniques (see Osterbrock 1989). Even when the physical conditions of the ionized gas such as electron temperature and density cannot be measured, the ratio of strong forbidden oxygen emission lines can still provide a measure of the overall metallicity of the gas (the so-called strong line  $R_{23}$  ratio method; Pagel *et al.* 1979; Kobulnicky, Kennicutt, & Pizagno 1999, hereafter KKP). However, in the DGSS and other large spectroscopic surveys, relative emission-line intensities are often not measured. Only equivalent widths are available. In a companion paper to this one, Kobulnicky & Phillips (2003) demonstrate that the ratio of emission-line equivalent widths,  $EW R_{23}$ , is a quantity comparable to  $R_{23}$  and is suitable for measuring oxygen abundances. We adopt the  $R_{23}$  calibration of McGaugh (1991) relating the ratio of [O III]  $\lambda\lambda$  4959, 5007, [O II]  $\lambda$ 3727, and H $\beta$  to the oxygen abundance relative to hydrogen, O/H. Although multiple prescriptions have been proposed in the literature, (reviewed in KKP and in Figure 5, the exact choice is unimportant here since we are only interested in *relative* abundances between local and distant galaxy samples analyzed in the same manner. Furthermore, the sample includes only luminous galaxies ( $M_B < -18$ , with three exceptions) so that, based on local analogs, they all are expected fall on the upper (metal-rich) branch of the empirical strong-line calibrations. The nine DGSS galaxies with measurable [N II] and H $\alpha$  lines all have [N II]/H $\alpha \gtrsim 0.1$ , confirming that these objects belong on the metal-rich branch of the calibration.<sup>5</sup> To ensure that the NFGS and KISS comparison objects are on the metal-rich branch, both local samples have been culled to contain only objects with  $F_{[N II]\lambda 6584}/F_{H\alpha} > 0.15$ .

In this paper, we compute oxygen abundances adopting the analytical expressions of McGaugh (1991, 1998 as expressed in KKP) which are based on fits to photoionization models for the metal-rich (upper) branch of the  $R_{23}$ -O/H relation. In terms of the reddening corrected line intensities,

---

<sup>5</sup>Adopting the less-plausible hypothesis that the DGSS galaxies lie on the metal-poor branch of the double-valued strong-line  $R_{23}$ -O/H relation would require all the galaxies to have extremely low oxygen abundances,  $12 + \log(O/H) < 8.0$ . Given that direct measurements of electron temperatures and oxygen abundances in similarly luminous  $z = 0.4$  objects rule out the lower branch possibility (Kobulnicky & Zaritsky 1999) we believe this upper-branch assumption to be generally valid.

this relation is

$$12 + \log(O/H) = 12 - 2.939 - 0.2x - 0.237x^2 - 0.305x^3 - 0.0283x^4 - \quad (3)$$

$$y(0.0047 - 0.0221x - 0.102x^2 - 0.0817x^3 - 0.00717x^4), \quad (4)$$

where

$$y \equiv \log(O_{32}) \equiv \log\left(\frac{I_{[O III]\lambda 4959} + I_{[O III]\lambda 5007}}{I_{[O II]\lambda 3727}}\right), \quad (5)$$

and

$$x \equiv \log(R_{23}) \equiv \log\left(\frac{I_{[O II]\lambda 3727} + I_{[O III]\lambda 4959} + I_{[O III]\lambda 5007}}{I_{H\beta}}\right). \quad (6)$$

Figure 5 shows graphically the relation between  $R_{23}$ ,  $O_{32}$  and oxygen abundance. Alternative relations from the literature are shown for comparison. A star marks the Orion nebula value (based on data of Walter, Dufour, & Hester 1992) which is in excellent agreement with the most recent solar oxygen abundance measurements of  $12 + \log(O/H)_{\odot} = 8.7$  (Prieto, Lambert, & Asplund 2001).

Kobulnicky & Phillips (2003) show that strong line equivalent width ratios are tightly correlated with flux ratios and can be used to obtain a metallicity-sensitive parameter akin to  $R_{23}$ . In our metallicity analysis we follow the prescriptions of Kobulnicky & Phillips (2003). Using equivalent widths, equations 5 and 6 become

$$y \equiv \log(EWO_{32}) \equiv \log\left(\frac{EW_{[O III]\lambda 4959} + EW_{[O III]\lambda 5007}}{EW_{[O II]\lambda 3727}}\right), \quad (7)$$

and

$$x \equiv \log(EWR_{23}) \equiv \log\left(\frac{EW_{[O II]\lambda 3727} + EW_{[O III]\lambda 4959} + EW_{[O III]\lambda 5007}}{EW_{H\beta}}\right). \quad (8)$$

As noted in Kobulnicky & Phillips (2003), the use of equivalent width ratios, rather than line flux ratios, has the particular advantage of being less sensitive to the (unknown) amount of extinction within the host galaxy, at least if the reddening toward the gas and stars is similar.<sup>6</sup>

---

<sup>6</sup>Calzetti, Kinney, & Storchi-Bergmann (1994) present evidence that this assumption may be invalid for some galaxies.

Table 1 records the oxygen abundances,  $12+\log(\text{O}/\text{H})$  derived from tabulated emission-line equivalent widths using the  $EW R_{23}$  prescription above. The galaxies range between  $12+\log(\text{O}/\text{H})=8.4$  and  $12+\log(\text{O}/\text{H})=9.0$ , with typical *random* measurement uncertainties of 0.03 to 0.10 dex. An additional uncertainty of  $\sim 0.15$  dex in  $\text{O}/\text{H}$ , representing uncertainties in the photoionization models and ionization parameter corrections for empirical strong-line calibration, should be added in quadrature to the tabulated measurement errors. There may also be zero-point shifts required to make this calibration directly comparable to standard solar oxygen abundances using meteoritic or solar photosphere measurements. The oxygen abundances derived here should *not* be compared to the canonical solar oxygen abundance ( $12+\log(\text{O}/\text{H})=8.89$ , Anders & Grevesse 1989;  $12+\log(\text{O}/\text{H})=8.69$ , Prieto, Lambert, & Asplund 2001) which is measured in a different manner. Our oxygen abundances may, however, be compared to local galaxies measured with the same empirical calibration technique to establish relative metallicity trends.

Figure 6 shows the relationship between redshift,  $M_B$ , B-V color<sup>7</sup>,  $EW_{H\beta}$ ,  $L_{H\beta}$ , and oxygen abundance for the 56 objects in our sample. Solid symbols distinguish objects by redshift: “low” (12 objects;  $0.26 < z < 0.40$ ), “intermediate” (20 objects;  $0.40 < z < 0.60$ ), and “high” (24 objects;  $0.60 < z < 0.82$ ). Dots, crosses, and 3-pointed triangles designate the KISS, K92, and NFGS local galaxy comparison samples. Here, as in Figure 3, the nearby comparison samples have been culled using the same emission-line selection criteria as the DGSS galaxies.

The redshift–luminosity panels of Figure 6 show a correlation. As expected for a flux-limited survey, more high luminosity objects and fewer low-luminosity objects are detected in the highest redshift bin compared to the lowest redshift bin. The DGSS galaxies are bluer than the mean NFGS galaxy, but consistent with the bluest local galaxies. The DGSS galaxies have, on average, larger emission line equivalent widths. The lower left panel compares the oxygen abundance versus redshift. The mean metallicity of the sample increases with redshift across the three bins. This trend is a consequence of the combined effects of the flux-limited sample and the luminosity-metallicity (L-Z) correlation for galaxies, pictured in the far-right column. The oxygen abundances of galaxies within each redshift bin correlate strongly with blue luminosity and less strongly with  $H\beta$  luminosity. There is no significant correlation between color and metallicity or between equivalent width and metallicity. The lower right panel reveals that the zero point of the L-Z correlation is displaced toward higher luminosities for larger redshifts. DGSS galaxies lie predominantly on the upper envelope of the local galaxy samples. While most of the DGSS sample galaxies are consistent with a luminosity-metallicity trend, the two least luminous objects, 092-1375 and 172-1242 with  $M_B \sim -16.5$ , lie well off the correlation if the empirical line-strength to-metallicity conversion is blindly applied. Based on studies of other galaxies of similar luminosity ( $M_B \simeq -16.5$ ; Skillman, Kennicutt, & Hodge 1989), we suspect that these two galaxies do not belong on the the upper branch of the  $R_{23}$ – $\text{O}/\text{H}$  relation. They lie in the “turn-around” region between the upper and lower branches where the strong-line calibration is particularly uncertain. If these objects lie on the lower

---

<sup>7</sup> $B - V$  colors for the DGSS, KISS, and NFGS are taken directly from published references.

branch of the  $R_{23}$  calibration, then they have metallicities near  $12+\log(\text{O}/\text{H})=8.1$ . Unfortunately neither of these objects have  $H\alpha$  or  $[\text{N II}]$  detections, so there is no way to discriminate between the two metallicity branches. Due to their metallicity ambiguity, we remove these two galaxies from any further analysis.

### 3.2. Comparison with Local Galaxies

We turn now to a detailed comparison of the luminous and chemical properties of the remaining DGSS sample to local galaxies and other intermediate-redshift galaxies. We select the same three sets of local galaxies. From the K92 sample, we use 22 comparison objects. From the photometry and spectroscopy presented in Jansen *et al.* (2000a,b) we selected a sub-sample of 36 NFGS objects using the same emission line criteria described above, including rejecting objects fainter than  $M_B = -17$ . From the KISS survey, we selected a sub-sample of 80 objects using the same emission-line and luminosity criteria which define our DGSS sample. To ensure that the NFGS and KISS comparison objects are on the metal-rich branch, both local samples have been culled to contain only objects with  $F_{[\text{N II}]\lambda 6584}/F_{H\alpha} > 0.15$ .

Figure 7 shows the luminosity-metallicity relation for DGSS galaxies compared to the three local galaxy samples. Filled symbols denote DGSS galaxies in the redshift ranges  $z = 0.26 - 0.4$ ,  $z = 0.4 - 0.6$ , and  $z = 0.6 - 0.82$  as in Figure 6. Crosses, skeletal triangles and dots denote the K92, the NFGS and the KISS local samples, respectively. The eight open squares show the best-measured objects in the  $0.6 < z < 1.0$  field galaxy study by Carollo & Lilly (2001; CL01).<sup>8</sup> Open circles and triangles show the  $z = 0.2 - 0.5$  objects from Kobulnicky & Zaritsky (1999; KZ99) which meet the same emission line selection criteria as the DGSS. Open stars are the high-redshift ( $z > 2$ ) galaxies from Kobulnicky & Koo (2000; KK00) and Pettini *et al.* (2001; Pe01). Lines represent least squares linear fits to the samples as shown in the key. Fits to local sub-samples are unweighted, whereas fits to the DGSS and high- $z$  sub-samples include the statistical uncertainties on O/H. A representative error bar in the lower right indicates the typical statistical uncertainties of  $\sigma(M_B) = 0.2$  mag and  $\sigma(\text{O}/\text{H}) = 0.12$  dex. It is worth emphasizing here that the oxygen abundances for each sample represented in Figure 7 have been computed in an identical manner from measured emission line equivalent widths. No corrections for internal reddening have been made. We have adopted the recommendation of Kobulnicky & Phillips (2003) and corrected all local and DGSS galaxy  $H\beta$  equivalent widths for  $2 \text{ \AA}$  of stellar Balmer absorption. The absolute B magnitudes have been computed (or converted from published values) assuming the  $H_0 = 70$ ,  $\Omega_M = 0.3$ ,  $\Omega_\Lambda = 0.7$  cosmology. K-corrections have been applied to the high-redshift samples based on multi-band rest-frame B-band and UV photometry. The various samples represented should be directly comparable, although they might not be completely representative of the entire population

---

<sup>8</sup>Magnitudes have been converted from the  $H_0 = 50$ ,  $\Omega_M = 1.0$  ( $q_0 = 0.5$ ) cosmology adopted in that study. Oxygen abundances are computed using the published  $R_{23}$  and  $O_{32}$  values from that work.

of galaxies at a given redshift.

Figure 7 reveals a striking variation in the zero point of the best fit luminosity-metallicity correlation with redshift of the sample. The slope also varies with redshift. Although considerable scatter exists within a given sub-sample, *the more distant galaxies are markedly brighter at a fixed oxygen abundance*. Equivalently, galaxies of a given luminosity are systematically more metal-poor at higher redshifts. Dashed lines show the linear least squares fits to the local NFGS samples using both O/H and  $M_B$  as the dependent variable. The heavy dashed line shows the linear bisector of the two fits and has the form:  $12 + \log(O/H) = -0.086 M_B + 7.14$ . The best fit to the local KISS galaxies in the upper panel is similar with  $12 + \log(O/H) = -0.12 M_B + 6.59$ . For the  $z \sim 0.7$  DGSS galaxies, we find  $12 + \log(O/H) = -0.16 M_B + 5.19$ .

Figure 7 underscores and extends the trend from Figure 6 by including galaxies at higher and lower redshifts. The most dramatic differences between the local and higher-redshift DGSS samples occur at the lower luminosities. At luminosities fainter than  $M_B = -19$ , the mean galaxy in the  $z = 0.60 - 0.82$  bin is a factor of 2 (0.2–0.3 dex) more metal poor than the NFGS or KISS local samples. At high luminosities, there is considerable overlap between all subsamples up to  $z = 0.8$ . At  $M_B = -21.5$ , the mean galaxy in the  $z = 0.60 - 0.82$  subset is perhaps only 0.1 dex more metal poor than the NFGS or KISS local samples, although the paucity of local galaxies prohibits a detailed comparison. The lack of DGSS galaxies in the lower right corner of the plot (low luminosity but high metallicity) represents a real offset from the local relation, and is not due any selection effect we can identify. Galaxies that might occupy this locus near  $M_B = -19$ ,  $12 + \log(O/H) = 8.7$  would have measurable emission lines and line ratios,  $R_{23}$ , identical to the more luminous galaxies with  $M_B = -21.5$ . Although the ratios of [O III] and [O II] line strengths to  $H\beta$  line strengths drop with increasing metallicity, the sample selection process would not preferentially exclude objects with low [O III]/ $H\beta$  (high metallicity) in favor of those with high [O III]/ $H\beta$  (low metallicity). If such low-luminosity, high-metallicity objects existed, they would have been detected and included in the analysis. In our selection of objects from the DGSS database, we found only 3 objects with measurable  $H\beta$  but immeasurably weak [O III]. In all those cases, poor sky subtraction is clearly the cause of the weak [O III]. Furthermore, there is no correlation between  $EW_{H\beta}$  and O/H (see Figure 6), as might be expected if selection effects had preferentially removed objects with weak line strengths from the sample or if the corrections for Balmer absorption dominated the errors in a systematic way.

We investigated other sources of systematic or selection effects by examining the residuals in the L-Z relation as a function of other fundamental galaxy parameters. Using unweighted linear least-squares fits to the KISS, NFGS, and DGSS samples separately, we computed residuals for each sample and searched for correlations with galaxy color,  $H\beta$  luminosity, size, and equivalent width. Only  $EW_{H\beta}$  is significantly correlated with L-Z residuals, and only for the DGSS galaxies. Figure 8 plots galaxy  $EW_{H\beta}$  versus luminosity residuals,  $\delta M_B$ , from a best-fit linear relation in the L-Z plane. There is no correlation for the KISS sample, or for the NFGS sample. There is a significant correlation for the intermediate- and high-redshift DGSS galaxies which is driven by

the handful of galaxies with  $EW_{H\beta} > 20 \text{ \AA}$ . This may plausibly be understood as a sign that the galaxies with large  $EW_{H\beta}$  are undergoing the strongest episodes of star formation, and are correspondingly offset to the bright side of the L-Z relation.

Comparing local galaxies having moderate  $EW_{H\beta}$  to the rare DGSS galaxies with uncommonly large  $EW_{H\beta}$  values could lead to misleading conclusions about the nature of distant versus local populations. With this in mind, we have constructed a new version of Figure 7 using only galaxies with  $EW_{H\beta} < 20 \text{ \AA}$  where the DGSS and local galaxies should be comparable. Figure 9 shows only those DGSS and local KISS, NFGS, and K92 galaxies with  $EW_{H\beta} < 20 \text{ \AA}$ . Although the number of DGSS data points are fewer, best fit lines to each sample show that the basic conclusion remains the same. DGSS galaxies in the high-redshift bin are as luminous as local galaxies at the luminous end of the L-Z relation, while the least luminous DGSS galaxies are, on average,  $\sim 1\text{--}2$  mag more luminous than local galaxies of comparable metallicity. Again, this result does not appear to be due to some kind of selection effect since the DGSS sample analyzed here spans the entire range of luminosities from the entire DGSS sample in each redshift interval, i.e., we are not simply selecting the brightest objects from each redshift interval, as shown by Figure 4.

Figure 4 hints at another kind of selection effect which may lead to erroneous conclusions regarding differences between DGSS and local galaxy samples. All of the DGSS galaxies have blue colors with  $B - V < 0.6$  while only a small fraction of the local galaxies are as blue. The DGSS samples are likely to contain a larger fraction of extreme star-forming galaxies with younger light-weighted stellar populations. As a second means of examining selection/population differences between the local and DGSS samples, we have constructed an alternative version of Figure 7 using only local galaxies with the bluest colors. Figure ?? shows only those DGSS and local KISS and NFGS galaxies with  $B - V < 0.6$ . Although the number of NFGS and KISS data points are fewer, best fit lines to each sample show that the basic conclusion remains the same. DGSS galaxies in the high-redshift bin are as luminous as local galaxies at the luminous end of the L-Z relation, while the least luminous DGSS galaxies are, on average,  $\sim 1\text{--}2$  mag more luminous than local galaxies of comparable metallicity.

As an even more stringent comparison, we considered only DGSS, NFGS, and KISS galaxies with  $EW_{H\beta} < 20 \text{ \AA}$  and  $B - V < 0.6$ . We further culled the local samples to remove objects with  $EW_{H\beta} < 10$ . The basic conclusion remains the same even for this very restrictive comparison designed to mitigate the color and EW differences between the DGSS and local samples. DGSS galaxies in the high-redshift bin are as luminous as local galaxies at the luminous end of the L-Z relation, while the least luminous DGSS galaxies are, on average,  $\sim 1\text{--}2$  mag more luminous than local galaxies of comparable metallicity.

A straightforward interpretation of Figure 7 and Figure 9 is that the least luminous emission line galaxies *have undergone considerable luminosity evolution*,  $\Delta M_B \simeq 1 - 2 \text{ mag}$ , from  $z \sim 0.7$  (7 Gyr ago) to the present and as much as  $\Delta M_B \simeq 3 - 4 \text{ mag}$  since  $z \sim 3$  (11 Gyr ago). This amount of brightening is consistent with the results of Ziegler *et al.* (2002) who found an evolution

of 1-2 mag in the Tully-Fisher relation for the least massive galaxies in their  $z = 0.1 - 1$  sample. An alternative way of understanding our result is to say that field galaxies with  $M_B \sim -18$  have experienced a measurable degree of metal enrichment (a factor of 2) at constant luminosity since  $z \sim 0.8$ . The arrows in Figure 9 indicate the evolution in the L-Z plane caused by constant star formation, passive evolution, metal-poor gas inflow, and star formation bursts and/or galaxy mergers. Some combination of these processes are responsible for evolving the  $z = 0.6 - 0.8$  galaxies into the region occupied by today’s  $z = 0$  galaxies.

The apparent evolution in the luminosity-metallicity relation seen in Figures 7 and 9 stands in contrast to the conclusions of Kobulnicky & Zaritsky (1999) and Carollo & Lilly (2001) who found little or no evolution in the redshift ranges  $0.1 < z < 0.5$  and  $0.5 < z < 1.0$ , respectively. Open squares in Figure 7 show that the CL01 objects fall at the high-luminosity end of the luminosity-metallicity correlation where the local and “distant” samples overlap. A comparison of the CL01 objects to the local NFGS sample would find that they are likely to be drawn from the same distribution, and hence the conclusion of CL01 is appropriate given the restricted nature of that sample. The new conclusion based on Figure 7 is made possible by the addition of larger numbers of galaxies and lower-luminosity galaxies which greatly extend the luminosity and metallicity baselines. Although the Kobulnicky & Zaritsky (1999) sample included a broader range of luminosities, the least luminous objects were at the lowest redshifts where offsets from local galaxies are least pronounced. Furthermore, Kobulnicky & Zaritsky (1999) used a local comparison sample that included only a restricted subset of galaxies from the Kennicutt (1992a,b) spectral atlas. Objects from this sample show increased scatter toward low-metallicities at fixed luminosity due, mostly, to the errors introduced by variable, unknown amounts of stellar Balmer absorption. The increased scatter in the local sample masked the trend which has now become apparent in Figure 7. This evolution of the L-Z relation between  $z = 0$  and  $z = 0.7$  supports the conclusions of Kobulnicky & Koo (2000), Pettini *et al.* (2001) and Mehlert *et al.* (2002) who found high redshift galaxies to be overly luminous for their metallicity at  $2.2 < z < 3.4$ .

## 4. Discussion

### 4.1. Modeling the Evolution in the L-Z Plane

The addition of chemical information on galaxies at earlier epochs provides a new type of constraint on theories of galaxy formation and evolution. If local effects such as the gravitational potential and “feedback” from supernova-driven winds are the dominant regulatory mechanisms for star formation and chemical enrichment, then the L-Z relation might be nearly independent of cosmic epoch. The semi-analytic models of Kauffman (1996) and Somerville & Primack (1999) show little or no evolution in the L-Z relation with epoch, although model-dependent prescriptions for stellar feedback and galactic winds are poorly constrained and may have large impacts on the chemical and luminous evolution. Based on the current understanding of cosmic evolution, that



the volume-averaged star formation rate was higher in the past (Pei & Fall 1995; Madau 1996), and that the overall metallicity in the universe at earlier times was correspondingly lower, we might expect galaxies to be considerably brighter at a given metallicity (i.e., luminosity evolution) if there was more primordial gas available in the universe to fuel star formation. A high- or intermediate-redshift galaxy sample ought to be systematically displaced from the local sample in the luminosity-metallicity (L-Z) plane *if individual galaxies reflect these cosmic evolution processes*, i.e., if they have an exponentially declining star formation rate since some epoch of formation, as commonly assumed, and/or if lower-mass galaxies evolve at different rates than high-mass galaxies. Comparison of the data from Figure 7 to some simple galaxy evolution models can help distinguish between these possibilities.

In a simple evolutionary model, galaxies begin as parcels of gas which form stars and produce metals as the gas fraction decreases from 100% to 0%. The B-band luminosity<sup>9</sup> is proportional to the star formation rate, which may vary as a function of time, but is generally believed to be proportional to the mass or surface density of the remaining gas (Kennicutt 1998). For a galaxy that evolves as a “closed box”, converting gas to stars with a fixed initial mass function and chemical yield, the metallicity is determined by a single parameter: the gas mass fraction,  $\mu = M_{gas}/(M_{gas} + M_{stars})$ . The metallicity,  $Z$ , is the ratio of mass in elements heavier than He to the total mass, and is given by

$$Z = Y \ln(1/\mu), \quad (9)$$

where  $Y$  is the “yield” as a mass fraction. A typical total metal yield for a Salpeter IMF integrated over 0.2–100  $M_{\odot}$  is  $Y = 0.012$  by mass (i.e., 2/3 the solar metallicity of 0.018; see Pagel 1997, Chapter 8).<sup>10</sup> A total oxygen yield for the same IMF would be  $Y_O = 0.006$ . Effective yields in many local galaxies seem to range from solar to factors of several lower, (Kennicutt & Skillman 2001; Garnett 2002), implying either that the nucleosynthesis prescriptions (e.g., Woosley & Weaver 1995) are not sufficiently precise, that assumptions about the form of the initial mass function are incorrect, or that metal loss is a significant factor in the evolution of galaxies. Garnett (2002) finds that oxygen yields of  $Y_O = 0.001$  to  $Y_O = 0.014$  among local irregular and spiral galaxies

---

<sup>9</sup>Here, we consider only the B-band luminosity-metallicity relation. Since young stars dominate the B-band luminosity, we expect that much of the scatter of the B-band L-Z relation is due to extinction and fluctuations in the star formation rate. Ideally, a rest-frame R-band or I-band luminosity-metallicity relation would be a more sensitive tool for evolution studies, since it will be less sensitive to these effects and eliminate the need for the color correction discussed in the previous section.

<sup>10</sup>We have assumed the solar oxygen abundance to be  $12 + \log(O/H)_{\odot} \simeq 8.7$  based on the new solar oxygen abundance determination of Prieto, Lambert, & Asplund (2001). This is 0.1-0.2 dex lower than the oft-adopted Anders & Grevesse (1989) value, but resolves the discrepancy between solar and Orion nebula oxygen abundances. For the Orion nebula,  $R_{23} = 0.70 \pm 0.03$ ,  $O_{32} \simeq 0.2 \pm 0.1$  (Walter, Dufour, & Hester 1992), which, given the calibration cited (Equation 3), leads to  $12 + \log(O/H) = 8.7 \pm 0.02$ , in excellent agreement with the Prieto, Lambert, & Asplund (2001) measurement.

are correlated with galaxy mass, suggesting an increasing amount of metal loss among less massive galaxies.

High-velocity winds capable of producing mass loss are observed in local starburst galaxies (e.g., Heckman *et al.* 2000) and in high-redshift Lyman break galaxies (Pettini *et al.* 2001), but the actual amount of mass ejected from galaxies is difficult to estimate. Simulations indicate that winds may be metal-enriched, such that metals are lost from galaxies more easily than gas of ambient composition (Vader 1987; De Young & Gallagher 1990; MacLow & Ferrara 1999). Recent Chandra observations of a local dwarf starburst galaxy, NGC 1569, provide the first direct evidence for metal-enhanced outflows (Martin, Kobulnicky, & Heckman 2002). Thus, the closed-box models are probably not appropriate and more realistic models including selective metal loss are required.

In order to compare the luminous and chemical evolution of galaxies in the L-Z plane to theoretical expectations, we ran a series of PÉGASE2 (Fioc & Rocca-Volmerange 1999) models. PÉGASE2 is a galaxy evolution code which allows the user to specify a range of input parameters including the initial mass function (which we take to be the Salpeter value, -2.35, between 0.1 and 120  $M_{\odot}$ , following Baldry *et al.* 2002), and the chemical yields (we assign Woosley & Weaver 1995 B-series models for massive stars). The effective metal yield of these models is  $Y = 0.016$ . For other critical parameters such as the star formation rate and the timescale on which the galaxy is assembled, we explored a range of formulations. We included an inclination averaged extinction prescription as implemented in PÉGASE2, but extinction changes the model B magnitudes negligibly by only 0.2 mag. Our goal in each case was to reproduce the qualitative behavior of Figure 7 where high-luminosity galaxies at  $z = 0.7$  occupy a similar locus as high-luminosity galaxies at  $z = 0$  and where low-luminosity  $z = 0.7$  galaxies are displaced toward brighter magnitudes and lower metallicities relative to their  $z = 0$  counterparts.

We tried a range of SFR prescriptions, including constant and exponentially declining star formation rates, for preconstituted galaxies of a fixed gas reservoir. In each case, both the initial star formation rate and total gas reservoir available had to be carefully tuned in an arbitrary manner to produce gas exhaustion at just the right epoch to account for the similarity of the  $z = 0.7$  and the local relations at the highest luminosities. By the time the evolution in the L-Z plane slowed when the gas supply neared exhaustion at  $\mu < 0.05$ , the model galaxies all had several times the solar metallicity, in conflict with the  $z = 0$  and  $z = 0.7$  observations.

We next tried a more physically motivated prescription, where the star formation rate is proportional to the mass of accumulated gas (or the gas density; Schmidt 1959; Kennicutt 1998). Galaxies are built by infall of primordial-composition gas with an infall rate that declines with an exponential timescale,  $\tau_{infall}$ , as implemented in PÉGASE2,

$$M(t) = M_{tot} \frac{e^{-t/\tau_{infall}}}{\tau_{infall}}. \quad (10)$$

We chose two representative gas infall timescales of 1 Gyr and 5 Gyr and two representative total

gas masses of  $10^{10} M_{\odot}$  and  $10^{11} M_{\odot}$ . A significant constraint on the models is the position of  $z \simeq 3$  Lyman break galaxies which lie 2-4 magnitudes brighter (0.5 dex more metal-poor) than the local L-Z relation. If the present-day emission-line samples are at all representative of the evolved descendants of the  $z = 0.7$  and  $z \simeq 3$  galaxies,<sup>11</sup> then a successful model must reproduce the rapid rise in metallicity and luminosity in the first 2-3 Gyr (as evidenced by the Lyman break galaxies), and it must reproduce the lack of significant L-Z evolution during the past 5-7 Gyr as evidenced by the similarity of the most luminous  $z = 0.7$  galaxies to the present-day L-Z relation. Furthermore, a successful model should indicate that the least luminous (least massive?) galaxies exhibit more pronounced luminosity and/or metallicity evolution during the last 7 Gyr than the more luminous objects in the sample. This means that the rate of evolution of the L-Z relation must be rapid during the first few Gyr of a galaxy’s formation, and then drop dramatically as a galaxy approaches the present-day L-Z relation. A slowing of luminous and/or chemical evolution of a galaxy must physically correspond either 1) to cessation of star formation and ultimately to depletion of the gas available to fuel star formation, or 2) to continued inflow of metal-poor gas which fuels star formation and dilutes the composition of the ISM so that a galaxy remains fixed in L-Z space.

Figure 11 shows evolutionary tracks of galaxies in the L-Z plane based on the infall PÉGASE2 models. The metallicity by mass,  $Z$ , is marked along the upper x-axis along with the corresponding gas mass fraction given by the models (equivalent to the gas mass fractions predicted by Equation 9 using a yield of 0.016) as a comparison. Pentagons in Figure 11 mark the model galaxies at ages of 1, 2, 4, 8, and 12 Gyr (from left to right). Dashed lines denote models with  $\tau_{infall} = 1$  Gyr and solid lines denote models with  $\tau_{infall} = 5$  Gyr. The upper set of curves shows galaxies with  $M_{tot} = 10^{11} M_{\odot}$  while the lower curves show galaxies with  $M_{tot} = 10^{10} M_{\odot}$ . These models produce the rapid rise in metallicity in the first few Gyr. These model masses are in good agreement with observational estimates which place lower limits on the masses of  $z \simeq 3$  Lyman break galaxies at  $few \times 10^{10} M_{\odot}$  (Kobulnicky & Koo 2000; Pettini *et al.* 2001) and indicate star formation rates of  $\sim 50 M_{\odot}/yr^{-1}$ . However, these models over-enrich the ISM at late times after 8 Gyr compared to the data. They predict gas mass fractions that are as low as 1% and metallicities as high as 3 times solar ( $Z=0.054$ ) after 12 Gyr, at odds with the observed properties of nearby galaxy samples. Lowering the model star formation rates would delay the chemical enrichment until later times and lower the luminosity at any given time.

As an experiment to produce models that better resemble the data, we introduced a metal yield efficiency parameter  $\eta_Z$  which reduces the effective yield of the models. Physically,  $\eta_Z$  may represent the fraction of metals retained in galaxies during episodes of wind-driven metal loss, or it may represent a correction to the theoretical yields from stellar populations. Figure 12 shows

---

<sup>11</sup>Most of the DGSS objects studied here have optical morphologies (see Figure 1) that qualitatively resemble disks, and their bulge-to-disk ratios are  $B/T \ll 1$ . Even if the current levels of star formation decline, their evolutionary descendants are likely to be systems with substantial disk components. Thus, it is plausible to think that the descendants of the  $z \sim 0.7$  DGSS galaxies are disk-like star-forming galaxies today, similar to the KISS and NFGS objects plotted in Figure 7.

the same models and data as Figure 11, except that the metal yield has been reduced by a factor of 2 ( $\eta_Z = 0.5$ ).<sup>12</sup> The  $M_{tot} = 10^{11} M_\odot$  model with  $\tau_{infall} = 1$  Gyr is now in better agreement with the  $z = 0.7$  and  $z = 0$  data at ages of 8-12 Gyr. However, the same model for  $M_{tot} = 10^{10} M_\odot$  becomes too metal-rich at ages of 8-12 Gyr compared to the  $z = 0$  data. The  $\tau_{infall} = 5$  Gyr provides a better fit to the  $z = 0.7$  and  $z = 0$  low-luminosity galaxies at these ages. Models with even longer infall timescales would lie even further to the left of the solid pentagons.

The evolution of the slope and zero point of the L-Z relation in Figure 12 is consistent with the idea that low-mass field galaxies assemble on longer timescales and require longer to reach high metallicities compared to their massive counterparts in the field.<sup>13</sup> Alternatively, the same results may be achieved if the low-mass galaxies begin their assembly process at a later cosmic epoch. There are not enough constraints in the models or the data to distinguish between these possibilities. In the context of the cold dark matter paradigm, the objects with the largest initial overdensities form first (e.g., Blumenthal *et al.* 1984; Navarro, Frenk, & White, 1995). Whether these first objects grow to become massive galaxies depends on the environment in which they are conceived. Initial galaxy cores which collapse in the vicinity of larger concentrations of baryonic matter grow to become the massive galaxies at the centers of today’s galaxy clusters. Objects that form in regions of lower cosmological overdensity would accrete gas on longer timescales and, if isolated from external influences, would proceed more slowly through the star formation and chemical evolution process. A longer formation timescale for lower mass field galaxies observed in the DGSS at  $z \sim 0.7$  can plausibly explain the observed evolution in the L-Z relation. Such a scenario, whereby galaxies assembly timescales vary with environment, is similar to that proposed by Sandage, Freeman, & Stokes (1970) to explain the differences along the Hubble sequence.

An additional free parameter not easily incorporated into the PÉGASE2 models is the role of starbursts on timescales of few Myr that occur in a galaxies evolving on long (Gyr) timescales according to the model prescriptions above. Studies of local galaxies show that their star formation histories are not smooth but instead are punctuated by periods of enhanced activity. Such short-term enhancements in the star formation rate of galaxies otherwise evolving smoothly can elevate the luminosity and emission line equivalent widths by factors of several. The observed emission line equivalent widths in DGSS galaxies average 10-20 Å, but some exceed 50! These characteristics would be better fit by superimposing a burst of star formation of  $\sim 10^{6-7} M_\odot$  on the model galaxies. The impact of instantaneous bursts on the evolution in the L-Z plane would be to create spikes along the model tracks toward higher luminosities. The amplitude of the spikes would scale with the amplitude of the burst, and could conceivably be several magnitudes and would persist for few 100

---

<sup>12</sup>This factor is not incorporated into the PÉGASE2 models in any self-consistent manner. Here we have simply reduced the final metallicity of the gas at each timestep by the factor  $\eta_Z = 0.5$ .

<sup>13</sup>Some galaxies, particularly dwarfs, may never exhaust their gas by the normal star formation process and may never reach high metallicities if the gas reservoir is cut off or removed prematurely by ram pressure stripping in a cluster environment or by galactic winds.

Myr. Given the morphological evidence for ongoing mergers among the DGSS sample, evidenced by inspection of Figure 1, it seems certain that short-term enhancements in the star formation rate are responsible for the more extreme luminosities and emission line equivalent widths among the sample. Examination of the PÉGASE2 models used here shows that as the  $EW_{H\beta}$  declines from 50 Å to 10 Å, the B-band luminosity drops by 0.7 mag. If we were to try to correct the magnitudes of the DGSS samples by some factor to account for their larger equivalent widths compared to the local samples, this factor would be less than 0.7 mag, not enough to account for the larger 1-2 mag offsets observed in the L-Z relations.

#### 4.2. A Hypothetical L-Z Relation with Redshift

Figure 13 shows schematically what the evolution in the L-Z plane may look like as a function of redshift. Lines at  $z = 0$  and  $z = 0.7$  are drawn to match the formal fits to the data in these redshift bins. The other hypothetical lines are drawn to indicate a possible evolutionary trend in the L-Z relation which is consistent with the (currently minimal) observational constraints. This schematic shows more clearly than Figure 12 the more pronounced evolution for low-mass galaxies compared to high mass galaxies and illustrates the increasingly rapid evolution at redshifts beyond  $z = 2$ . Figure 13 may be approximated by an analytical function which expresses metallicity in terms of luminosity,  $M_B$ , and redshift,  $z$  as

$$12 + \log(O/H) = [(-0.095z) - 0.13] M_B + (-2.31z + 6.18). \quad (11)$$

In terms of the metallicity by mass,  $Z$ , an equivalent expression is

$$\log Z = [(-0.21z) - 0.10] M_B + (-4.9z - 6.9), \quad (12)$$

where  $\log Z_{\odot} = -1.74$ .

Because this schematic is based upon observations of luminous ( $M_B < -18$ ), metal-rich ( $12 + \log(O/H) > 8.3$ ) galaxies, it may be inapplicable to the least luminous, metal-poor galaxies where the behavior of the L-Z relation may change (e.g., Melbourne & Salzer 2002). Extrapolation beyond the current luminosity and redshift data is imprudent.

## 5. Conclusions

Observations of star-forming galaxies from the Deep Extragalactic Evolutionary Probe (DEEP) survey of Groth Strip galaxies in the redshift range  $0.26 < Z < 0.82$  show a correlation between B-band luminosity and oxygen abundance, like galaxies in the local universe. The L-Z relations for  $z < 0.8$  intersects with the L-Z relation at  $z = 0$  for the most luminous ( $M_B < -20.5$ ) DGSS

and local galaxies. There appears to be very little evolution in the L-Z plane among these most luminous galaxies over the last 8 Gyr. However, less luminous (and by implication, possibly less massive) galaxies are 1-2 mag more luminous at  $0.6 < z < 0.8$  than  $z = 0$  galaxies of similar metallicity. Said another way, galaxies of comparable luminosity are 0.1-0.2 dex more metal-rich at  $z = 0$  compared to  $z = 0.7$ . The least luminous galaxies appear to undergo considerable evolution in the L-Z plane. This differential evolution can be explained in one of two ways. Either less luminous (less massive?) galaxies are assembled on longer timescales than the super  $L^*$  galaxies, or they begin their formation process at a later cosmic epoch. Evolution of galaxies in the L-Z plane over the redshift range  $z = 3$  to  $z = 0$  appears to be a combination of fading and chemical enrichment for plausible models. Loss of up to 50% of the oxygen appears to be necessary to avoid over-enriching the galaxies at the observed redshifts. Because the local comparison sample has been selected on the same emission-line basis as the intermediate-redshift samples, accounting for differences in color, this result is consistent with evolution in the luminous and chemical properties of star-forming galaxies over the last 4-8 Gyr.

How does this result compare to conclusions about the evolution of the luminosity function (LF)? Lin *et al.* (1999) use early CNOC2 data on  $> 2000$  galaxies over the redshift range  $0.12 < z < 0.55$  to conclude that, among late-type galaxies (the ones most comparable to the DGSS objects selected here), changes in the LF are most consistent with *density* evolution, and little or no *luminosity evolution*. However, Cohen (2002), based on studies in the Hubble Deep Field North vicinity over the redshift range  $0.01 < z < 1.5$ , concluded that emission-line objects show *moderate luminosity evolution* and *little density evolution*. Interpreting Figure 5 of Lin *et al.* (1999) as luminosity evolution suggests that, between  $z \simeq 0.70$  and  $z \simeq 0.20$ , late-type galaxies with  $M_B = -19$  fade by  $\simeq 1$  mag, while galaxies with  $M_B = -21$  fade by  $\simeq 0.2$  mag. This is qualitatively and quantitatively consistent with the amount of fading required for the  $z = 0.7$  DGSS galaxies to match the local L-Z relation in the models in Figure 12.

These results imply that  $z \sim 0.6 - 0.8$  DGSS galaxies must have significantly higher (20%-80%) gas mass fractions than comparably luminous local galaxies. Such a difference in the mean gas mass fractions of galaxies would, in principle, be observed with instruments such as the proposed radio-wave square kilometer array. New optical and near-IR spectroscopic observations can test the schematic predictions of Figure 13 by measuring oxygen abundances of objects fainter than  $M_B \sim -20.5$  in the critical redshift range  $z = 1$  to  $z = 2$  (i.e., by filling in the low-luminosity side of Figure 12).

We thank John Salzer for insightful conversations and for providing the KISS data in electronic form, Shiela Kannappan for a helpful discussion about the NFGS, Matt Bershady and James Larkin for scientific inspiration. Detailed reading by an anonymous referee greatly improved this manuscript. H. A. K was supported by NASA through grant #HF-01090.01-97A awarded by the Space Telescope Science Institute which is operated by the Association of Universities for Research in Astronomy, Inc. for NASA under contract NAS 5-26555 and by NASA through NRA-00-01-

LTSA-052. This work was also made possible by NSF grants AST95-29098 and AST00-71198 and NASA/HST grants AR-07532.01, AR-06402.01, and AR-05801.01.

## REFERENCES

- Anders, E., & Grevesse, N. 1989, *GeCoA*, 53, 197
- Baldry, I. K. *et al.* 2002, *ApJ*, 569, 582
- Baldwin, J. A., Phillips, M. M., & Terlevich, R. 1981, *PASP*, 93, 5
- Bergeron, J., & Stasinska, G. 1986, *A&A*, 169, 1
- Bershady, M. A., Haynes, M. P., Giovanelli, R., & Andersen, D. R. 1988, in *Galaxy Dynamics*, eds. D. R. Merritt, M. Valluri, & J. A. Sellwood (ASP Conf Series)
- Blumenthal, G. M., Faber, S. M., Primack, J. R., & Rees, M. J. 1984, *Nature*, 311, 517
- Brodie, J. P., & Huchra, J. P. 1991, *ApJ*, 379, 157
- Calzetti, D., Kinney, A. L., & Storchi-Bergmann, T. 1994, *ApJ*, 429, 582
- Carollo, C. M. & Lilly, S. J. 2001, *ApJ*, 548, L153 (CL01)
- Cohen, J. G. 2002, *ApJ*, 567, 672
- De Young, D. S., & Gallagher, J. S. III 1990, *ApJ*, 356, L15
- Djorgovski, S., & Davis, M. 1987, *ApJ*, 313, 59
- Dopita, M. A., & Evans, I. N. 1986, *ApJ*, 307, 431
- Dressler, A., Lynden-Bell, D., Burstein, D., Davies, R. L., Faber, S. M., Terlevich, R. J., & Wegner, G. 1987, *ApJ*, 313, 42
- Edmunds, M. G. & Pagel, B. E. J. 1984, *MNRAS*, 211, 507
- Faber, S. M. 1973, *ApJ*, 179, 423
- Fioc, M. & Rocca-Volmerange, B. 1999, *astro-ph/9912179*
- Forbes, D. A., Phillips, A. C., Koo, D. C., & Illingworth, G. D. 1995, *ApJ*, 462, 89
- French, H. B., 1980, *ApJ*, 240, 41
- Garnett, D. R. 2002, *ApJ*, 581, 1019
- Gebhardt, K., Faber, S. M., Koo, D. C., Im, M., Simard, L., Illingworth, G. D., Phillips, A. C., Sarajedini, V. L., Vogt, N. P., & Willmer, C. N. A. 2003, *ApJ*, in press
- Groth, E. J., Kristian, J. A., Lynds, R., O’Neil, E. J. Jr., Balsano, R., & Rhodes, J. 1994, *BAAS*, 185
- Heckman, T. M. 1980, *A&A*, 87, 152
- Heckman, T. M., Lehnert, M. D., Strickland, D. K., & Armus, L. 2000, *ApJS*, 129, 493

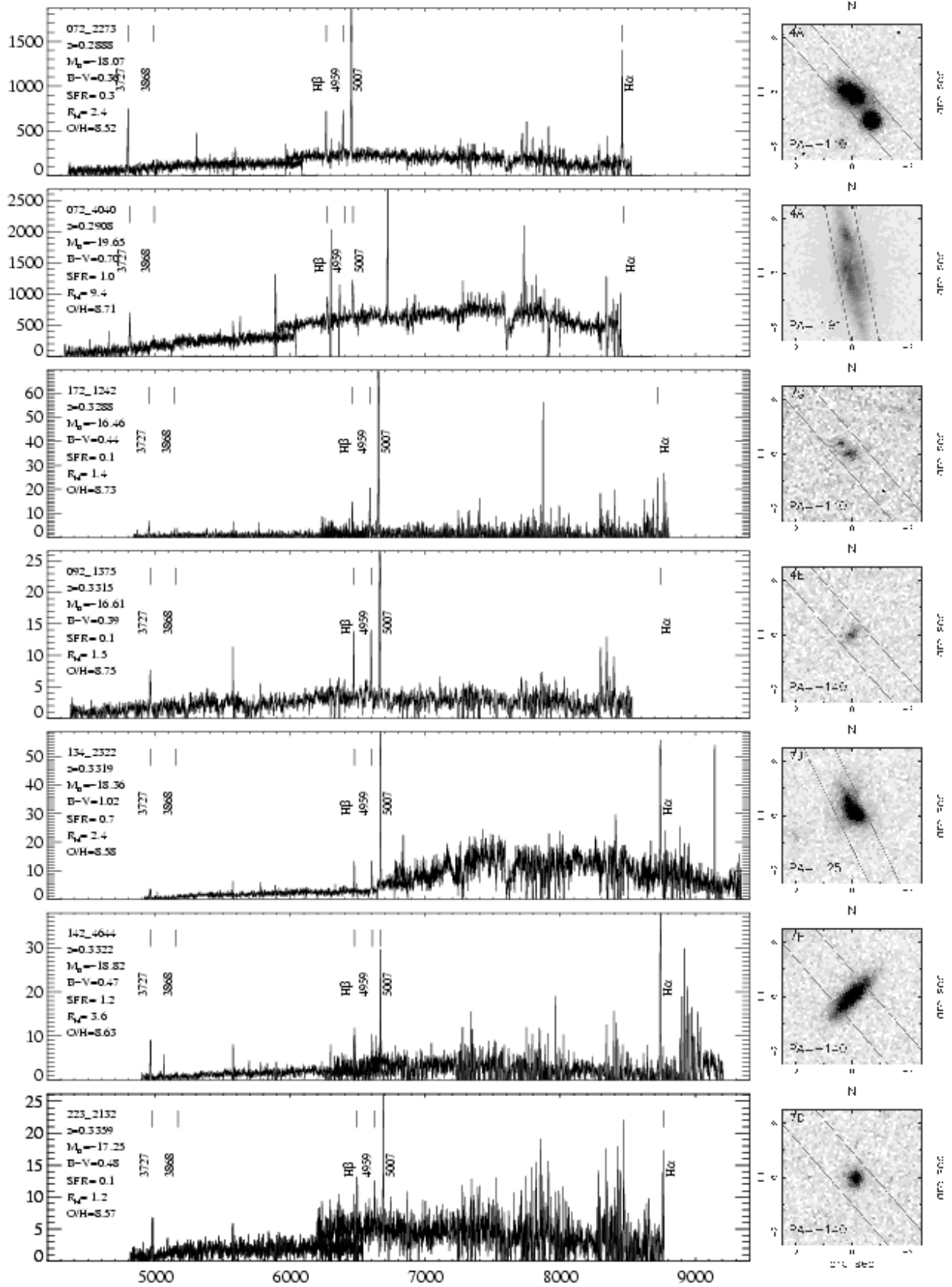
- Huchra, J. P., Davis, M., Latham, D., & Tonry, J. 1983, ApJS, 52, 89
- Im, M., Simard, L., Faber, S. M., Koo, D. C., Gebhardt, K., Willmer, C. N. A., Phillips, A. C., Illingworth, G. D., Vogt, N. P., & Sarajedini, V. L. 2002, ApJ, 571, 136
- Jansen, R. A., Franx, M., Fabricant, D., & Caldwell, N. 2000a, ApJS, 126, 271 (NFGS)
- Jansen, R. A., Fabricant, D., Franx, M., & Caldwell, N. 2000b, ApJS, 126, 331
- Kannappan, S. J., Fabricant, D. G., & Franx, M. 2002, AJ, 123, 2358
- Kauffman, G. 1996, MNRAS, 281, 475
- Kelson, D. D., van Dokkum, P. G., Franx, M., Illingworth, G., & Fabricant, D. 1997, ApJ, 478, L13
- Kennicutt, R. C. Jr. 1983, ApJ, 272, 54
- Kennicutt, R. C. Jr. 1992a, ApJS, 79, 255
- Kennicutt, R. C. Jr. 1992b, ApJ, 388, 310
- Kennicutt, R. C. Jr. 1998, ApJ, 498, 541
- Kennicutt, R. C. Jr. & Skillman, E. D. 2001, AJ, 121, 1461
- Kinney, A. L., Calzetti, D., Bohlin, R. C., McQuade, K., Storchi-Bergmann, T., & Schmitt, H. R. 1996, ApJ, 467, 38
- Kobulnicky, H. A., Kennicutt, R. C., & Pizagno, J. 1998, ApJ, 514, 544
- Kobulnicky, H. A. & Koo, D. C. 2000, ApJ, 545, 712 (KK00)
- Kobulnicky, H. A. & Phillips, A. C. 2003, ApJ, 000 (KP03)
- Kobulnicky, H. A. & Zaritsky, D. 1999, ApJ, 511, 118 (KZ99)
- Lequeux, J., Peimbert, M., Rayo, J. F., Serrano, A., & Torres–Peimbert, S. 1979, A&A, 80, 155
- Lin, H., Yee, H. K., Carlberg, R. G., Morris, S. L., Sawicki, M., Patton, D. R., Wirth, G., & Shepard, C. W. 1999, ApJ, 518, 533
- Lilly, S. J., Le Fèvre, O., Hammer, F., & Crampton, D. 1996, ApJ, 460, L1
- Lilly, S. J., Tresse, L., Hammer, F., Crampton, D., & Le Fèvre, O. 1995, ApJ, 455, 108
- Lilly, S. J., *et al.* 1998, ApJ, 500, 75
- Lu, L., Sargent, W. L. W., Barlow, T. A., 1997, ApJ, 484, 131
- MacLow, M. M. & Ferrara, A. 1999, ApJ, 513, 142
- Madau, P., Ferguson, H., Dickinson, M., Giavalisco, M., Steidel, C., & Fruchter, A. 1996, MNRAS, 283, 1388
- Marzke, R. O., da Costa, L. N., Pellegrini, P. S., Willmer, C. N. A., Geller, M. J. 1998, ApJ, 503, 617
- Martin, C. L., Kobulnicky, H. A., & Heckman, T. M. 2002, ApJ, 574, 663

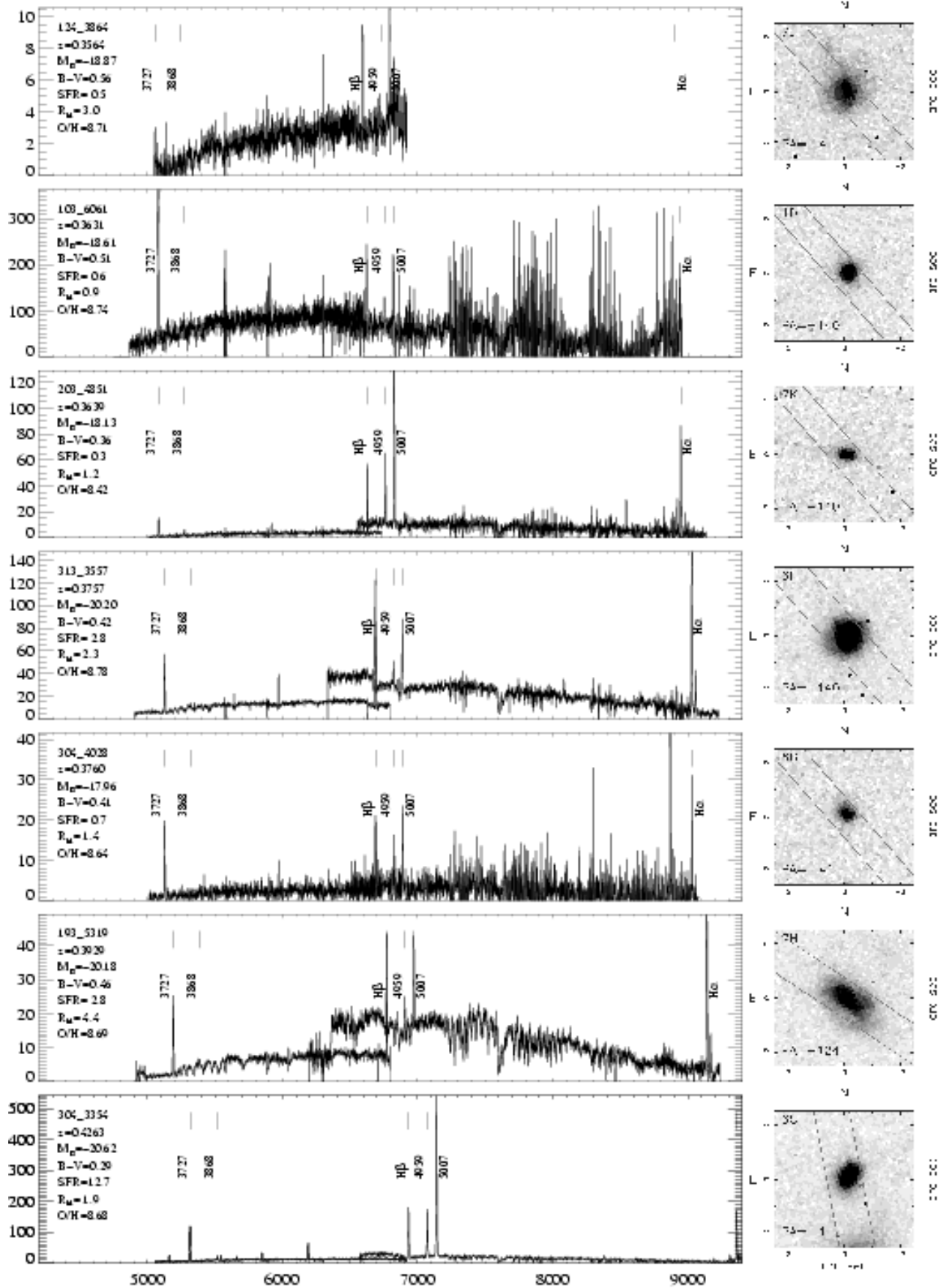


- McCall, M. L., Rybski, P. M., & Shields, G. A. 1985, *ApJS*, 57, 1 (MRS)
- McGaugh, S. 1991, *ApJ*, 380, 140
- McGaugh, S. 1998, private communication
- Mehlert, D. *et al.* 2002, *A&A*, 393, 809
- Melbourne, J., & Salzer, J. J. 2002, *AJ*, 123, 2302
- Navarro, J. P., Frenk, C. S., & White, S. D. M. 1995, *MNRAS*, 275, 561
- Norberg, P., *et al.* (The 2dFGRS Team), 2002, *MNRAS*, 336, 907
- Oke, J. B., *et al.* 1995, *PASP*, 107, 375
- Osterbrock, D. E. 1989, *Astrophysics of Gaseous Nebulae and Active Galactic Nuclei*, University Science Books:Mill Valley CA
- Pagel, B. E. J. Edmunds, M. G., Blackwell, D. E., Chun, M. S., & Smith, G. 1979, *MNRAS*, 189, 95
- Pagel, B. E. J. 1997, “Nucleosynthesis and Chemical Evolution of Galaxies”, Cambridge University Press
- Pei, Y. C., & Fall, S. M. 1995, *ApJ*, 454, 69
- Pettini, M., Shapley, A. E., Steidel, C. C., Cuby, J.-G., Dickinson, M., Moorwood, A. F. M., Adelberger, K. L., & Giavalisco, M. 2001, *ApJ*, 554, 981 (Pe01)
- Pettini, M., Smith, L. J., King, D. L., Hunstead, R. W. 1997, *APJ*, 486, 665
- Prieto, C. A., Lambert, D. L., & Asplund, M. 2001, *ApJ*, 556 L63
- Prochaska, J. X. & Wolf, A. M. 1999, *ApJS*, 121,369
- Richer, M. G., & McCall, M. L. 1995, *ApJ*, 445, 642
- Rola, C. S., Terlevich, E., & Terlevich, R. J. 1997, *MNRAS*, 289, 419
- Roche, N., Ratnatunga, K., Griffiths, R. E., Im, M., & Naim, A. 1998, *MNRAS*, 293, 157
- Salzer, J. J., Gronwall, C., Lipovetsky, V. A.; Kniazev, A., Moody, J. W., Boroson, T. A., Thuan, T. X., Izotov, Y. I., Herrero, J. L., Frattare, L. M. 2000, *AJ*, 120, 80 (KISS)
- Sandage, A., Freeman, K. C., & Stokes, N. R. 1970, *ApJ*, 160, 831
- Sarajedini, V. L., & the DEEP Team, 2003, in prep. (Paper XIII).
- Sargent, W. L. W., Steidel, C. C., & Boksenberg, A. 1988, *ApJS*, 68, 539
- Sawicki, M. J., Lin, H., & Yee, H. K. 1997, *AJ*, 113, 1
- Schade, D., Carlberg, R. G., Yee, H. K., & Lopez-Cruz, O. 1996a, *ApJ*, 464, 63
- Schade, D., Carlberg, R. G., Yee, H. K., & Lopez-Cruz, O. 1996b, *ApJ*, 465, 103
- Schmidt, M. 1959, *ApJ*, 129. 243
- Simard, L., & Pritchett, C. J. 1998, *ApJ*, 505, 96

- Simard, L., Koo, D. C., Faber, S. M., Sarajedini, V. L., Vogt, N. P., Phillips, A. C., Gebhardt, K., Illingworth, G. D., & Wu, K. L. 1999, *ApJ*, 1999, 519, 563
- Simard, L., Willmer, C. N. A., Vogt, N. P., Sarajedini, V. L., Phillips, A. C., Koo, D. C., Im, M., Illingworth, G. D., Gebhardt, K., & Faber, S. M. 2002, *ApJS*, 142, 1 (Paper II)
- Skillman, E. D., Kennicutt, R. C., & Hodge, P. 1989, *ApJ*, 347, 875
- Somerville, R. S., & Primack, J. R. 1999, *MNRAS*, 310, 1087
- Steidel, C. C. 1990, *ApJS*, 74, 37
- Trager, S. C., Worthey, G., Faber, S. M., Burstein, D., & Gonzalez, J. J. 1998, *ApJS*, 116, 1
- Tully, R. B., & Fisher, J. R. 1977, *A&A*, 54, 661
- Vader, P. 1987, *ApJ*, 317, 128
- van Dokkum, P. G., & Franx, M. 1996, *MNRAS*, 281, 985
- Veilleux, S., & Osterbrock, D. E. 1987, *ApJS*, 63, 295
- Vogt, N., Forbes, D., Phillips, A. C., Gronwall, C., Faber, S. M., Illingworth, G. D., & Koo, D. C. 1996, *ApJ*, 465, L15
- Vogt, N., Phillips, A. C., Faber, S. M., Gallego, J., Gronwall, C., Guzman, R., Illingworth, G., Koo, D. C., & Lowenthal, J. D. 1997, 479, L121
- Vogt, N. *et al.* 2002, *ApJ*, in prep, (Paper I)
- Walter, D. K., Dufour, R. J., & Hester, J. J. 1992, *ApJ*, 397, 196
- Woosley, S. E. & Weaver, T. A. 1995, *ApJS*, 101, 181
- Zaritsky, D., Kennicutt, R. C., & Huchra, J. P. 1994, *ApJ*, 420, 87
- Ziegler, B. L., Böhm, A., Fricke, K. J., Jäger, K., Nicklas, H., Bender, R., Drory, N., Gabasch, A., Saglia, R. P., Seitz, S., Heidt, J., Hehlert, D., Möllenhoff, C., Noll, S., & Sutorius, E. 2002, *ApJ*, 564, L69
- Zucca, E. *et al.* ESO Slice Project team 1997, *A&A*, 326, 477

Fig. 1.— Unfluxed spectra for 66 emission-line galaxies culled from the DEEP survey of the Groth Strip using the criteria discussed in Section 2 along with their HST F814W images. Object are ordered by redshift, as in Table 1, with the 10 possible or probable AGN at the end. Markings identify major emission lines of the [O II] $\lambda$ 3726/29 doublet, [Ne III]  $\lambda$ 3868, H $\beta$ , [O III] $\lambda\lambda$ 4959,5007, and, where applicable, H $\alpha$ . Other positive features are generally residuals from night sky lines which could not be completely subtracted. Each panel shows two different spectra, obtained with “red” and “blue” grating settings. Seven-digit strings in the upper left give the DGSS identification number. Rectangles on the images show spectroscopic slit positions. (All 10 panels appear in the electronic edition only).





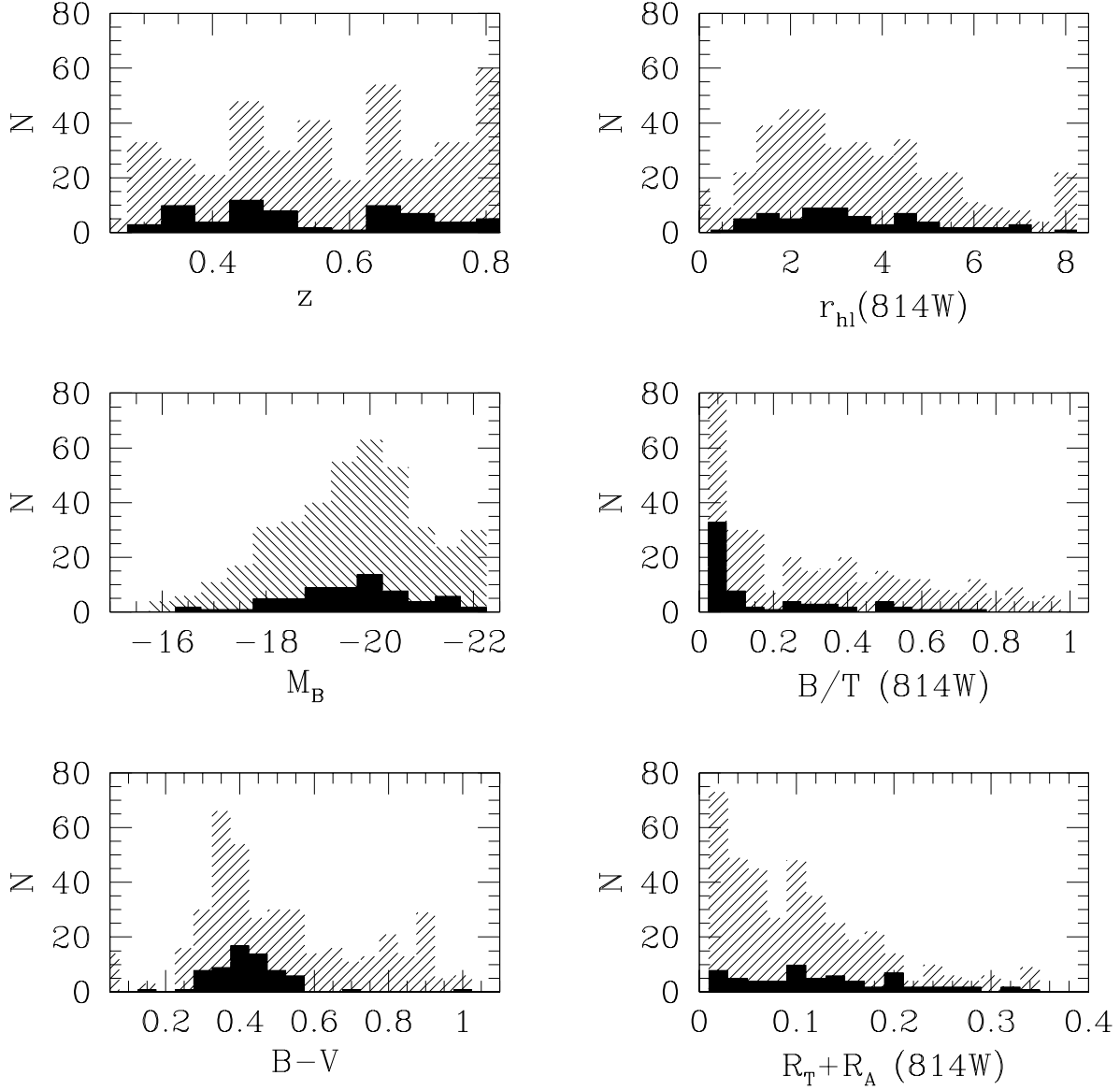


Fig. 2.— Histogram of 66 galaxies selected for chemical analysis (filled) compared to the total 398 objects in the survey with  $0.26 < z < 0.82$ . We show the distribution as a function of redshift,  $M_B$ , B-V color, half-light radius  $R_{hl}$ , bulge fraction  $F_{bulge}$ , and asymmetry index,  $R_T + R_A$ . This figure demonstrates that galaxies selected as suitable for chemical analysis are representative of the larger DGSS sample in the same redshift range in terms of their redshift distributions, sizes, luminosities and bulge fractions. However, the 66 selected galaxies preferentially have the bluest B-V colors and the most asymmetric morphologies.

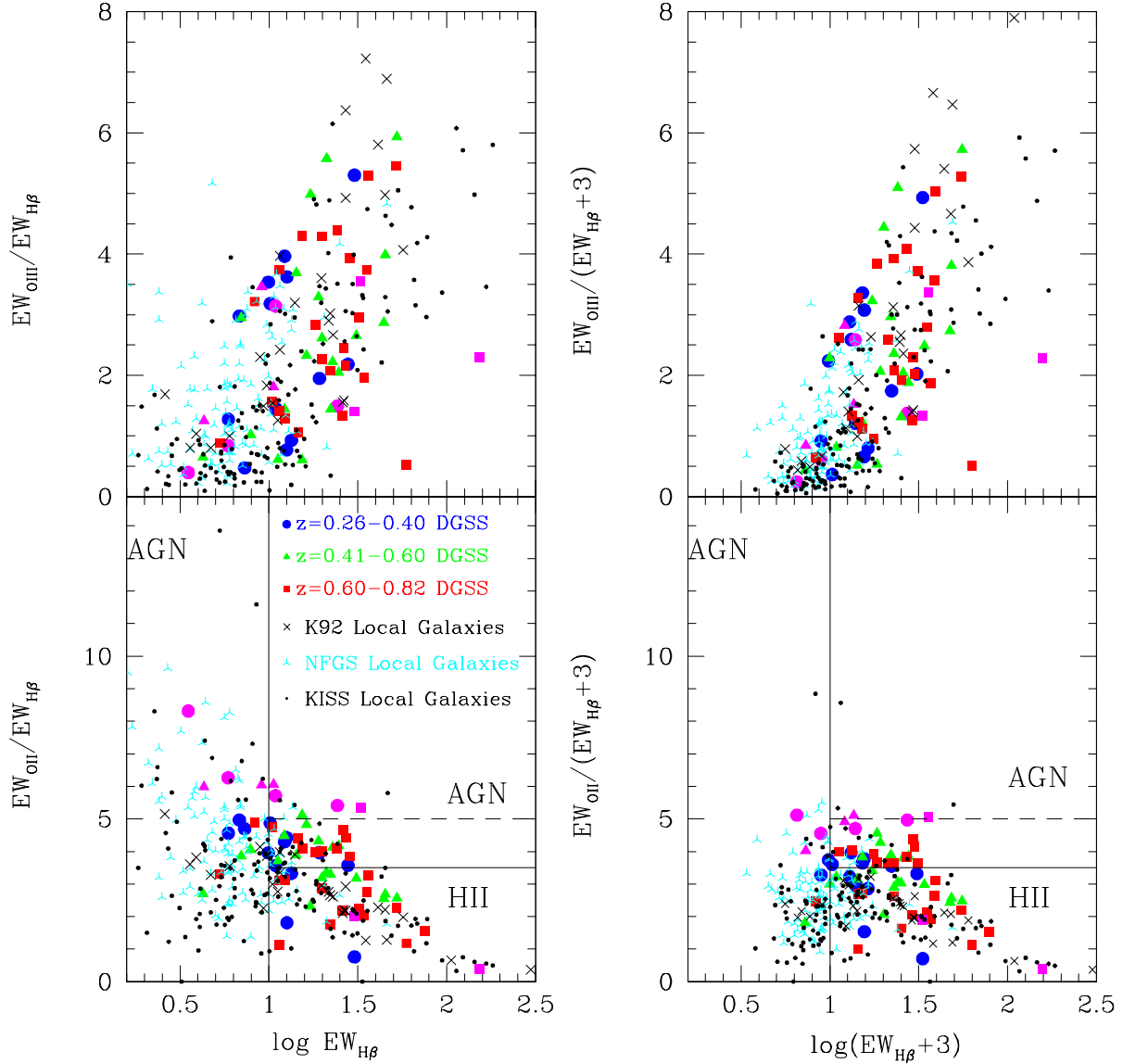


Fig. 3.— Diagnostic diagrams,  $EW_{[O II]}/EW_{H\beta}$  versus  $\log EW_{H\beta}$ , for the identification of AGN and starforming galaxies based on Rola *et al.* (1997). The full NFGS and KISS local samples are shown. AGN typically occupy the upper left and upper right sectors while starforming H II galaxies typically fall in the lower right regions, as divided by solid lines. The lower left sector is occupied by both normal galaxies with low star formation rates and some AGN. Open symbols show a comparison sample of local galaxies drawn from Kennicutt (1992b) and the NFGS (Jansen *et al.* 2000). Filled symbols coded by redshift denote the new objects presented here. On the left we plot the raw equivalent width data, while on the right we add  $3 \text{ \AA}$  to the  $EW_{H\beta}$  as a rough correction for underlying Balmer absorption in stars. On the basis of this diagram we identify and remove from the sample 8 DGSS galaxies (magenta-colored) with  $EW_{[O II]}/EW_{H\beta} > 5$  (dashed lines) as possible AGN or objects with large, unconstrained amounts of stellar Balmer absorption.

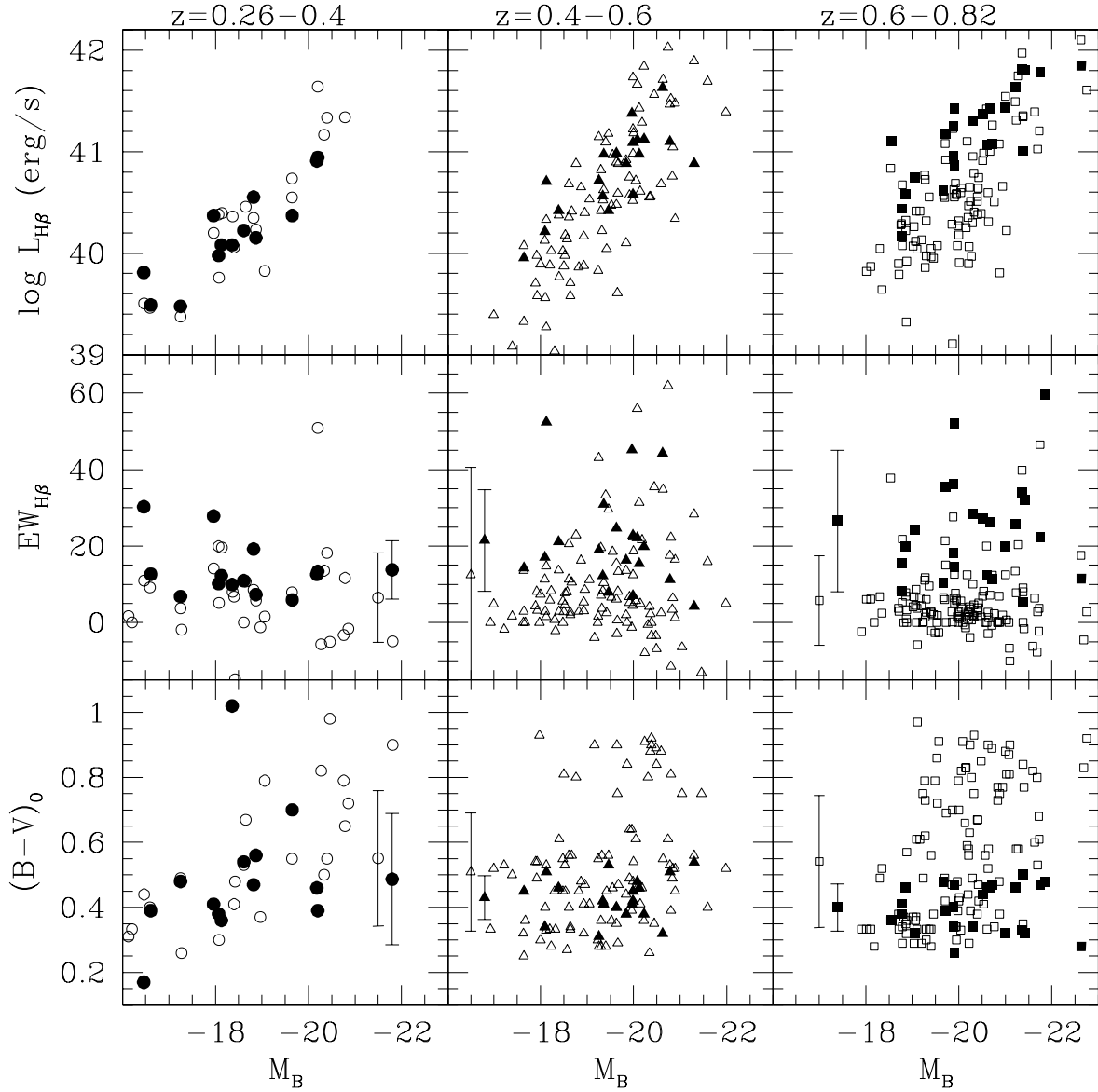


Fig. 4.— A comparison of the luminosity, color, and emission line strength for 56 galaxies selected for chemical analysis (solid symbols) to the 276 DGSS galaxies with emission lines (open symbols) selected from among the 398 DGSS galaxies in the  $0.26 < z < 0.82$  range. Error bars shows means and dispersions for the subsamples. Objects are binned by redshift. Galaxies selected for analysis in the lowest redshift bin are representative of the DGSS objects in that redshift interval. However, galaxies selected for analysis from the highest redshift bins are biased toward the bluest colors and highest emission line equivalent widths. The correlation between  $M_B$  and  $L_{H\beta}$  luminosity is an artifact produced by computing  $L_{H\beta}$  from  $M_B$  and  $EW_{H\beta}$ .



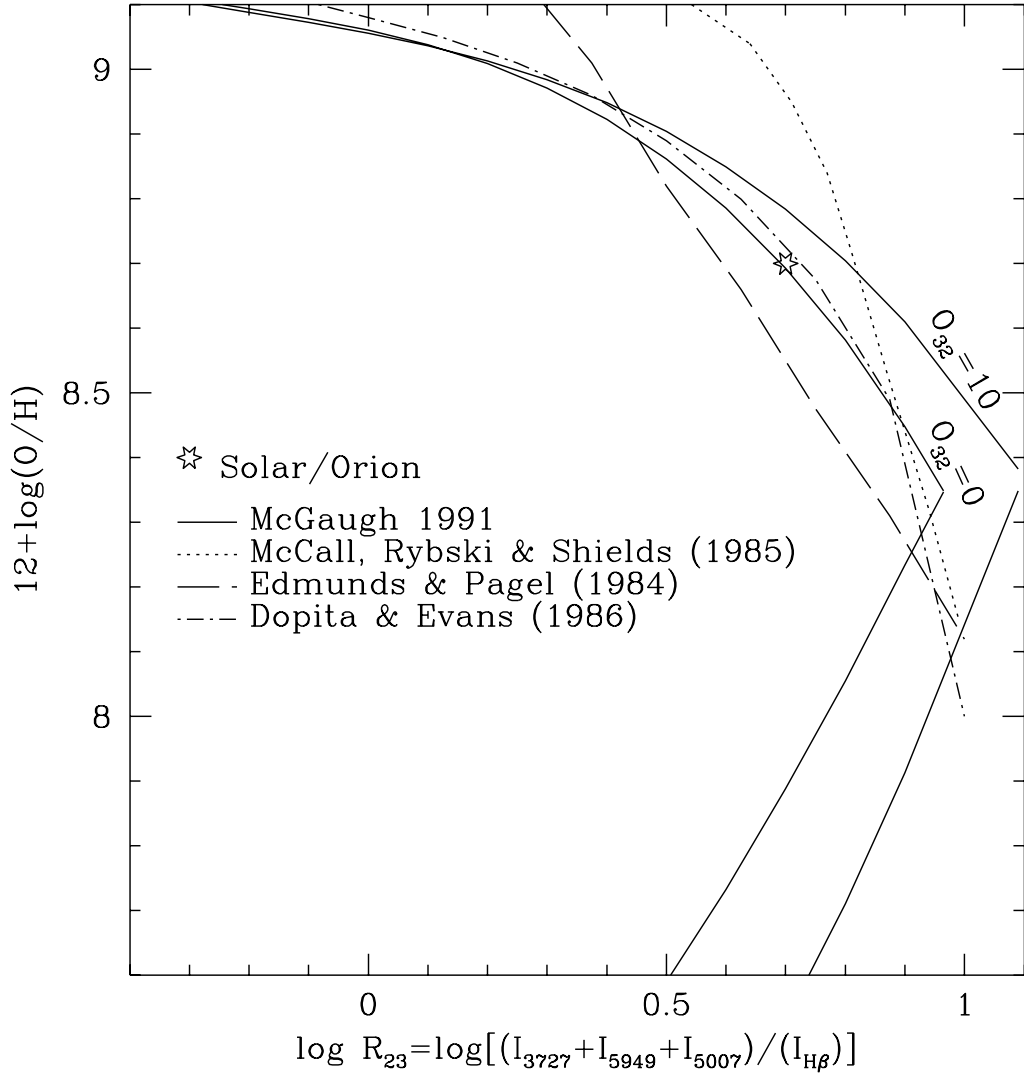


Fig. 5.— Relation between the emission line ratio,  $\log R_{23} \equiv \log[(I_{3727} + I_{4959} + I_{5007}) / (I_{H\beta})]$ , and oxygen abundance,  $12+\log(O/H)$  for a variety of calibrations from the literature. We adopt an analytical expression from McGaugh (1991) which takes into account the ionization parameter as measured by the  $O_{32}$  ratio. A star marks the Orion nebulae oxygen abundance (Walter, Dufour, & Hester 1992) which is consistent with the solar abundance, based on the recent measurement by Prieto, Lambert, & Asplund (2001).

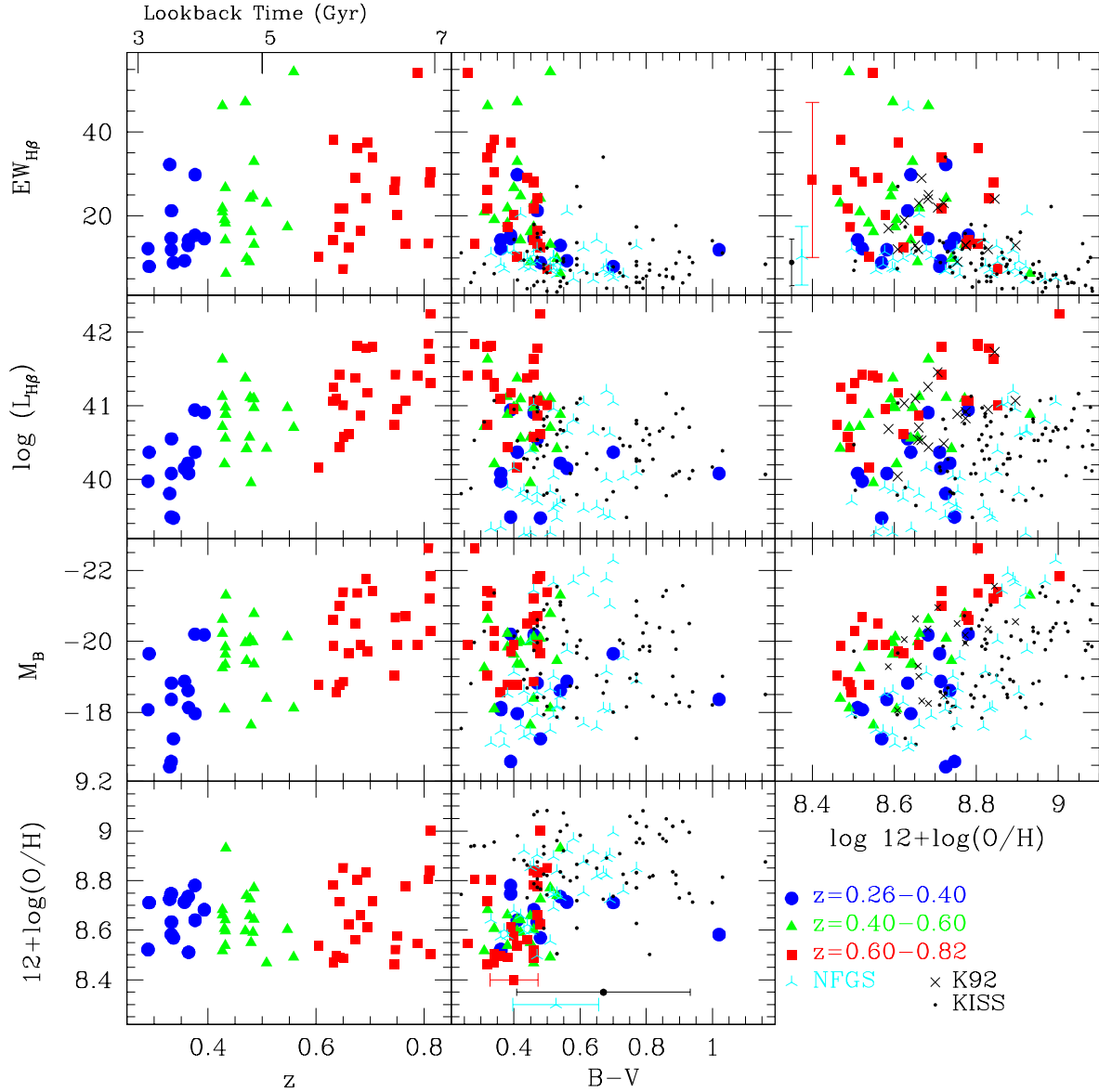


Fig. 6.— Relation between redshift,  $M_B$ , B-V color,  $EW_{H\beta}$ ,  $L_{H\beta}$ , and  $12+\log(\text{O}/\text{H})$  for 56 DGSS galaxies with subsets of the NFGS, K92, and KISS samples chosen to match the DGSS emission line ratio criteria. Points with error bars in some panels compare the means and dispersions in color and  $EW_{H\beta}$  for the DGSS, NFGS, and KISS samples. DGSS galaxies in the highest redshift bin are preferentially bluer with higher star formation rates and larger emission line equivalent widths. Each redshift interval exhibits a correlation between metallicity and both blue and  $H\beta$  luminosities, but with different zero points. There is no significant correlation between metallicity and color, or between metallicity and emission line equivalent width.

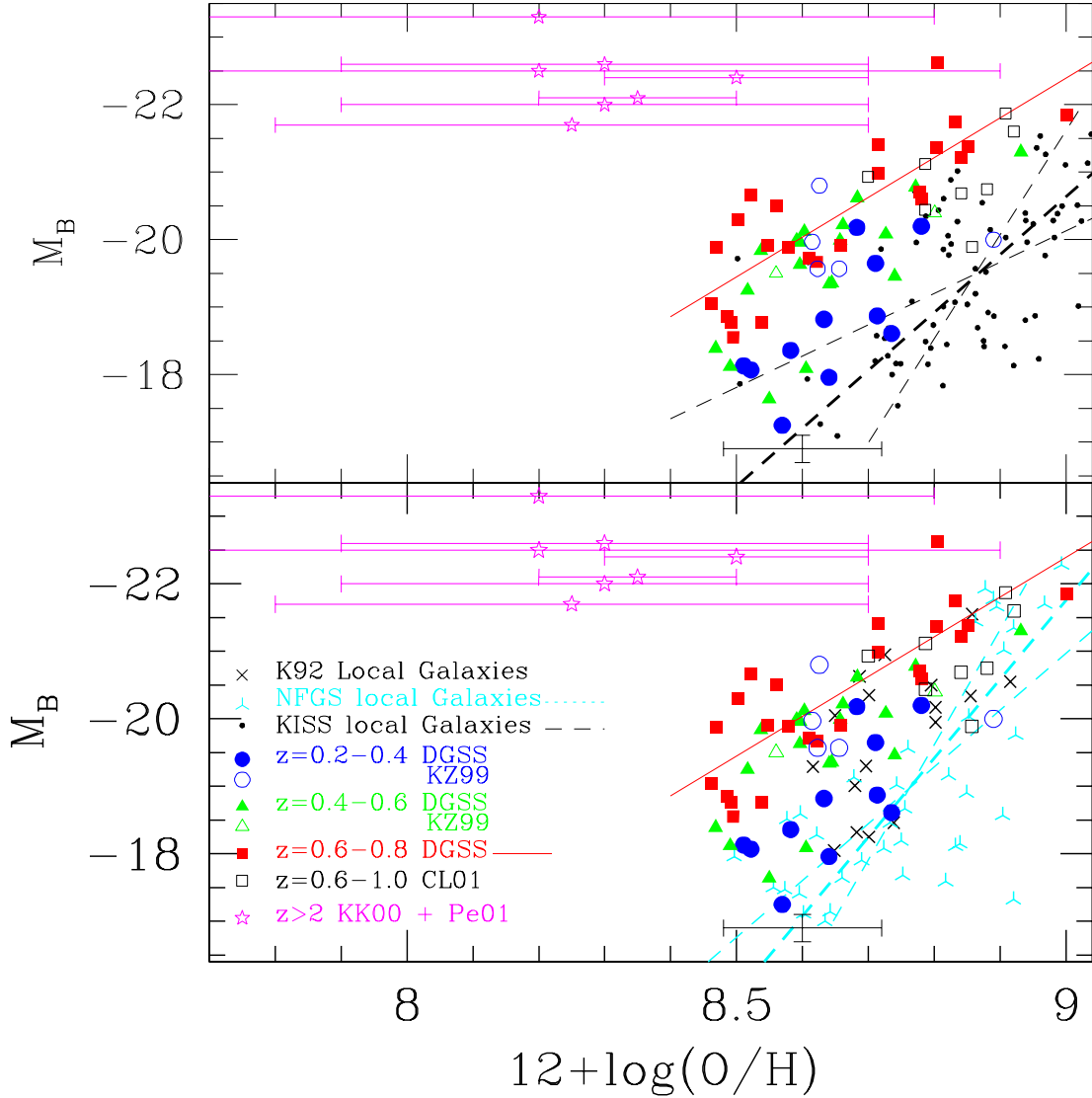


Fig. 7.— Luminosity-metallicity (L-Z) relation including samples of local  $z < 0.1$  galaxies from the NFGS, KISS, and Kennicutt (1992b) catalogs, with intermediate-redshift DGSS objects from this study (filled symbols) and the Carollo & Lilly (2001) and Kobulnicky & Zaritsky (1999) compilations (open symbols). A representative error bar is shown. Stars denote high-redshift objects (Kobulnicky & Koo 2000; Pettini *et al.* 2001) with error bars representing the full permitted range of metallicities ( $\sim 3\sigma$ ). The intermediate-redshift L-Z relation is consistent with the local L-Z relation for luminous galaxies, but diverges toward lower metallicity. Residuals from the local L-Z relation are most pronounced for low-luminosity DGSS galaxies in the highest redshift bin. This is consistent with the hypothesis that the most massive objects complete their evolution more rapidly, and the least massive objects evolve more slowly.

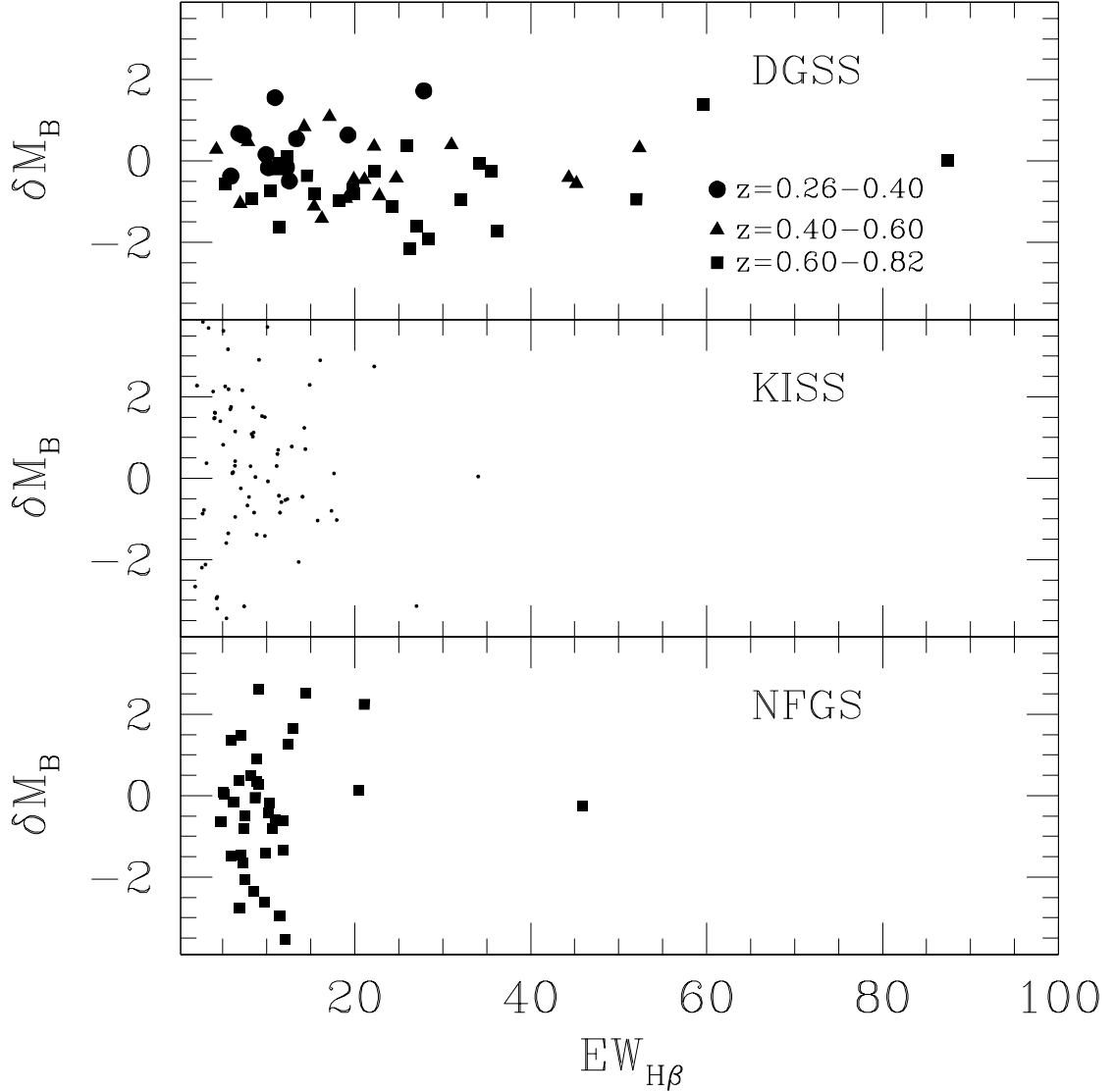


Fig. 8.— Galaxy  $EW_{H\beta}$  versus luminosity residuals,  $\delta M_B$ , from a best-fit linear relation in the L-Z plane for the DGSS, KISS, and NFGS samples. There is no correlation between  $EW_{H\beta}$  and L-Z residuals for the local samples. There is a weak correlation among the DGSS galaxies, driven mostly by the few galaxies with extremely large  $EW_{H\beta}$ . We searched for other parameters, including galaxy color and size, which might correlate with L-Z residuals and explain some of the dispersion in the L-Z relation, but no significant correlations were found.

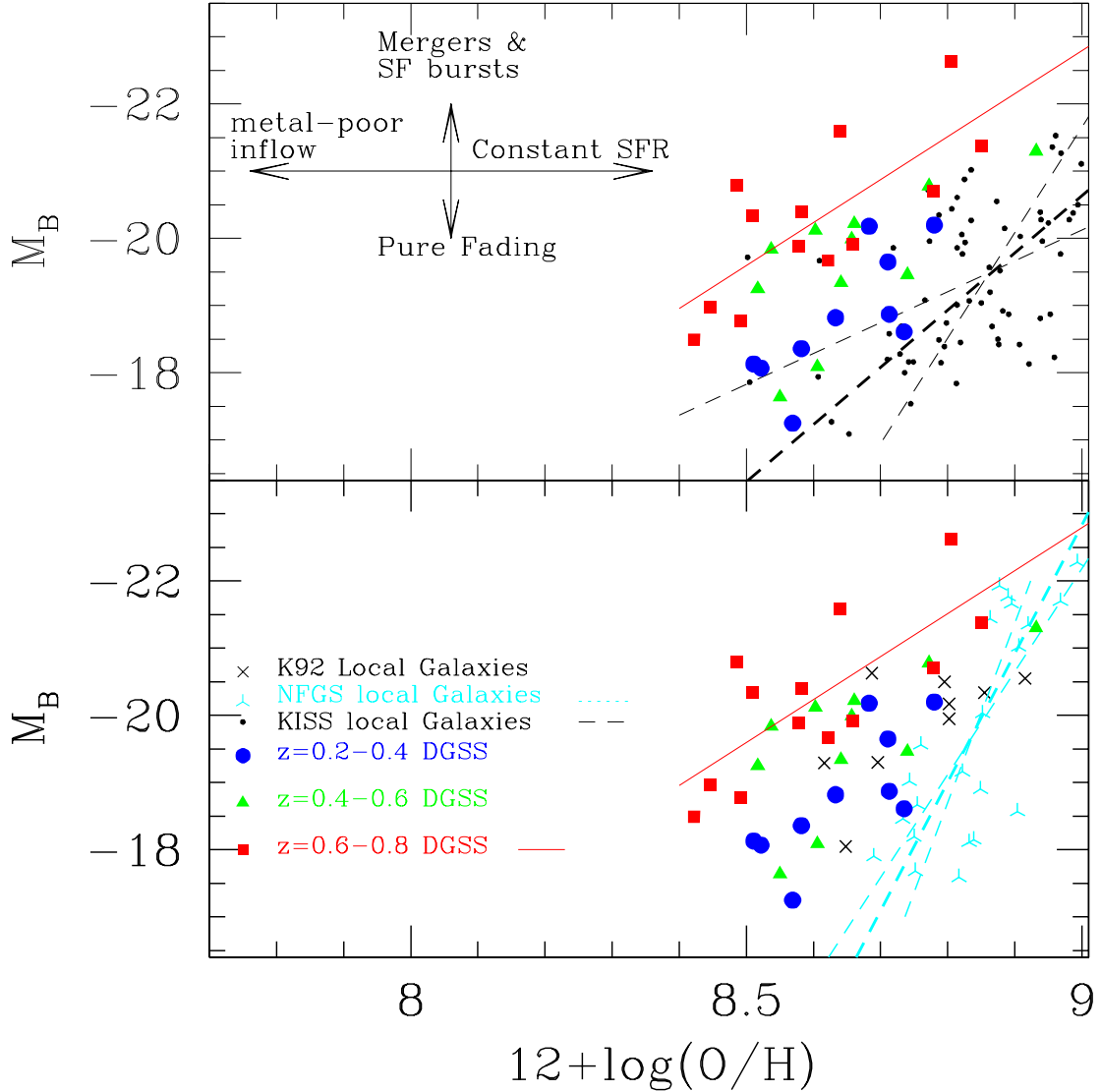


Fig. 9.— Luminosity-metallicity (L-Z) relation showing only local and DGSS galaxies with  $EW_{H\beta} < 20 \text{ \AA}$ . Here again, the most luminous DGSS galaxies are as luminous as the local galaxies of comparable metallicity, while the least luminous DGSS galaxies are  $\sim 1 - 2$  mag brighter than local galaxies of comparable metallicity. The schematic at left indicates the evolution in the L-Z plane caused by constant star formation, passive evolution, metal-poor gas inflow, and star formation bursts and/or galaxy mergers. Some combination of these processes are responsible for evolving the  $z = 0.6 - 0.8$  galaxies into the region occupied by today’s  $z = 0$  galaxies.

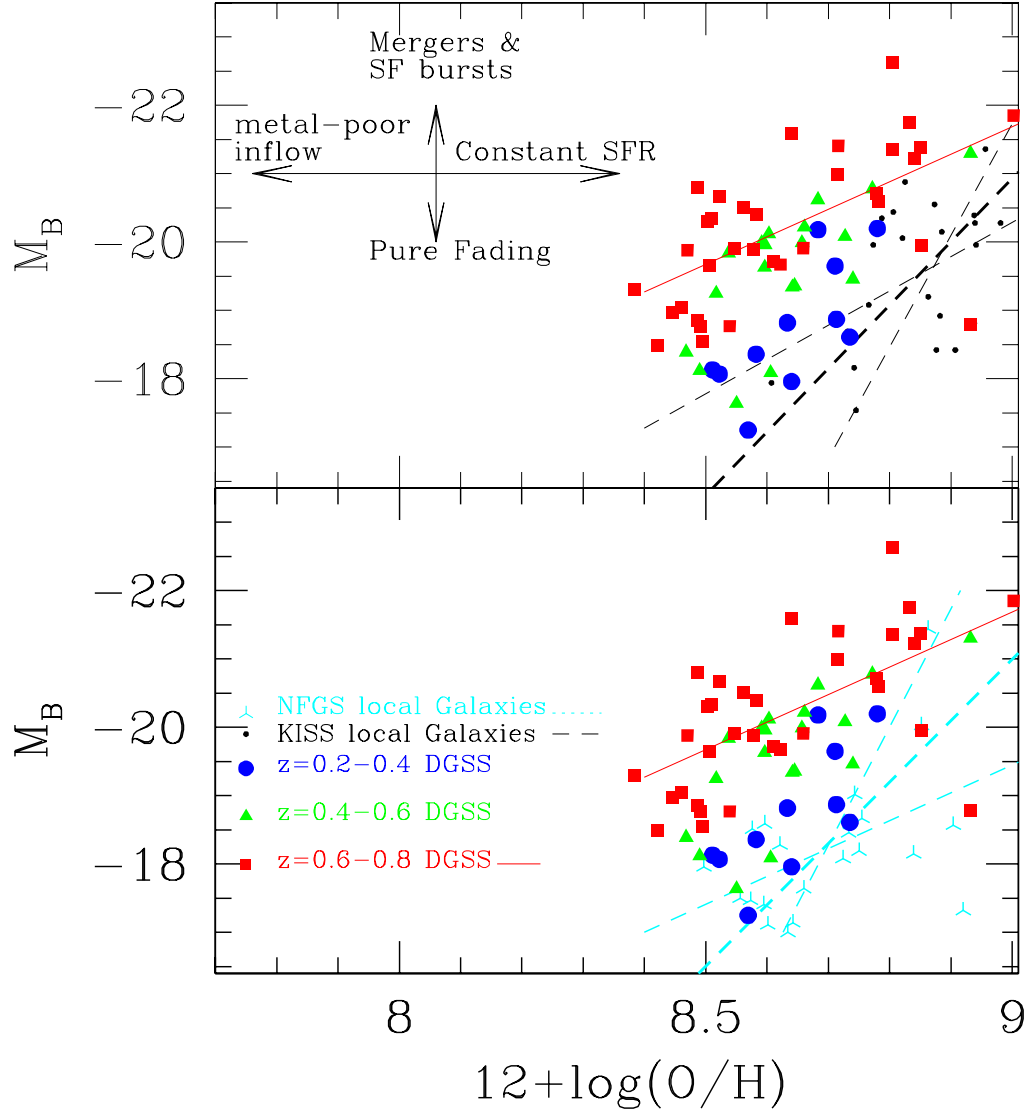


Fig. 10.— Luminosity-metallicity (L-Z) relation showing only local and DGSS galaxies with  $B-V < 0.6 \text{ \AA}$ . Here again, the most luminous DGSS galaxies are as luminous as the local galaxies of comparable metallicity, while the least luminous DGSS galaxies are  $\sim 1-2$  mag brighter than local galaxies of comparable metallicity.

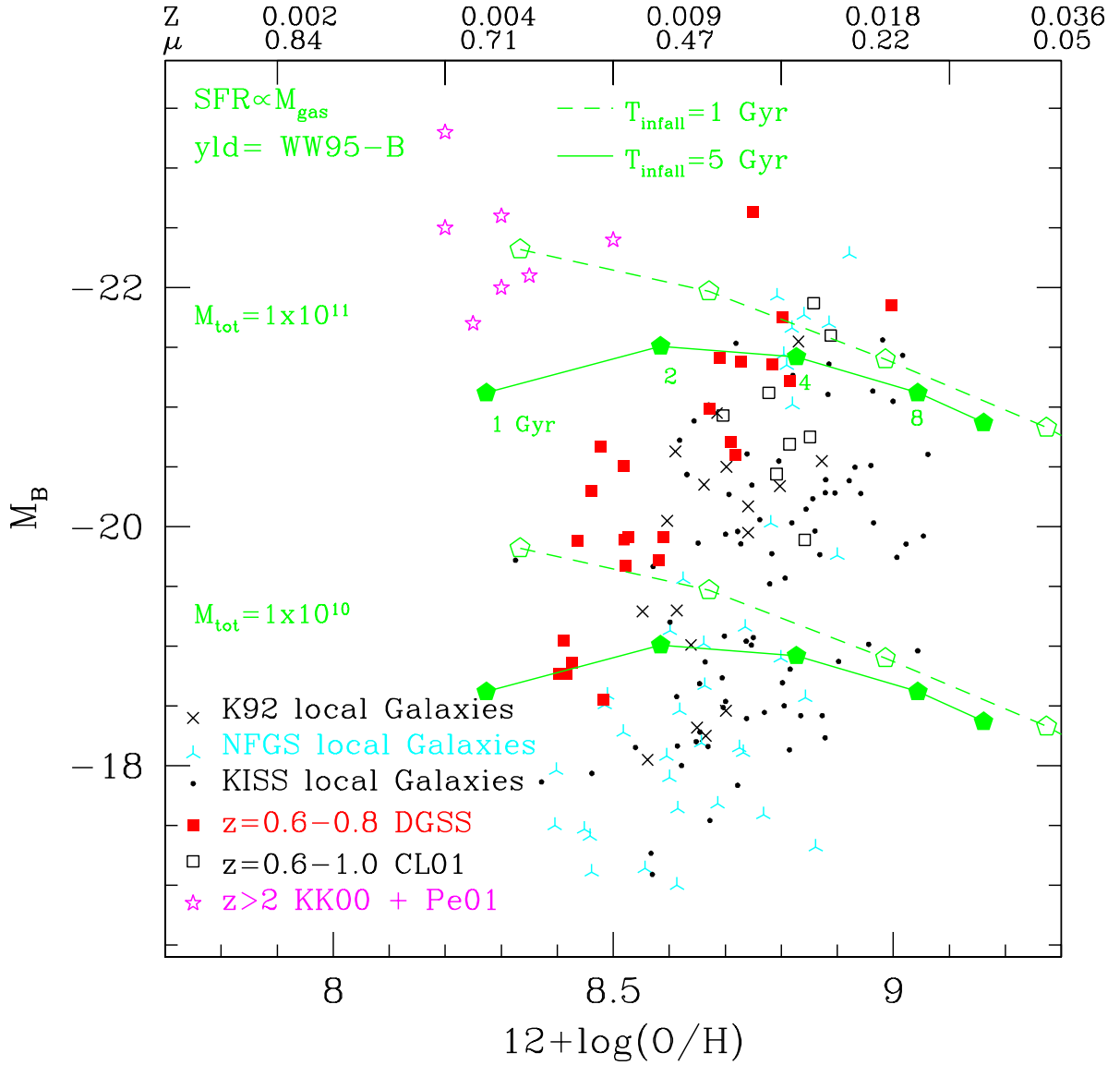


Fig. 11.— L-Z relation with a subset of the symbols from Figure 7. Lines and pentagons show the evolution of a model galaxy with a star formation rate proportional to the gas mass where the galaxy is built by exponentially-decreasing infall of primordial gas with infall timescale of 1 Gyr and 5 Gyr. Pentagons denote galaxies at 2, 4, 8, and 12 Gyr. Galaxy masses of  $10^{10} M_{\odot}$  and  $10^{11} M_{\odot}$  are shown. The top of the figure shows the corresponding gas metallicity,  $Z$ , and mass fraction,  $\mu$ , assuming a closed-box scenario for an effective yield of 0.012 from Weaver & Woosley (1995) series B models. The relative offset of low-mass  $z = 0.6 - 0.8$  galaxies from the local L-Z relation can be understood as the result of a longer gas infall timescale or a later formation epoch for low-mass galaxies compared to high-mass galaxies.

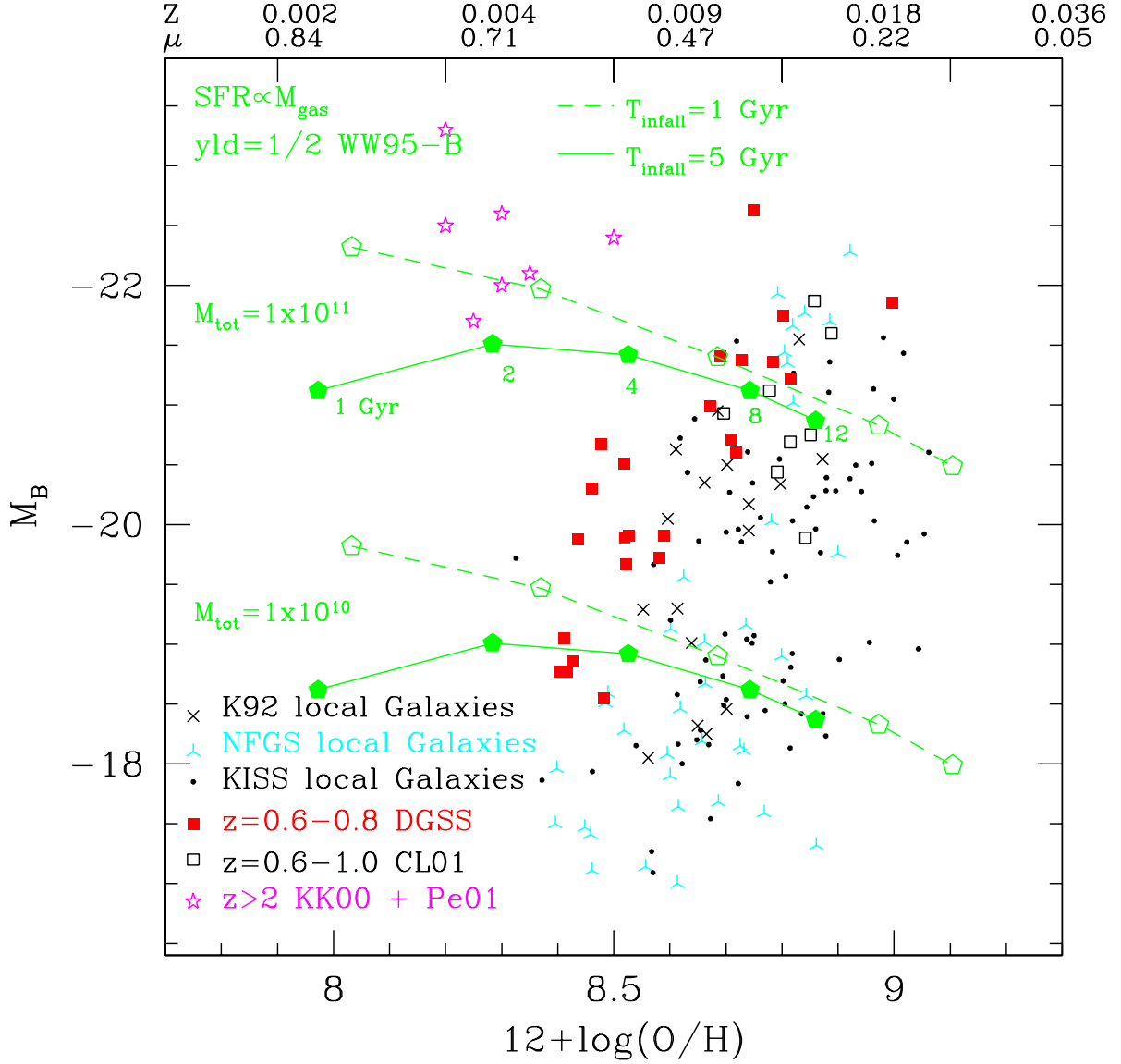


Fig. 12.— Comparison of data to evolutionary models in the L-Z plane similar to Figure 11, except that the effective yield of the models has been arbitrarily reduced by a factor of 2. The metallicities of the reduced-yield models do not rise as quickly, do not overproduce metals at late times, and are in better agreement with the data.



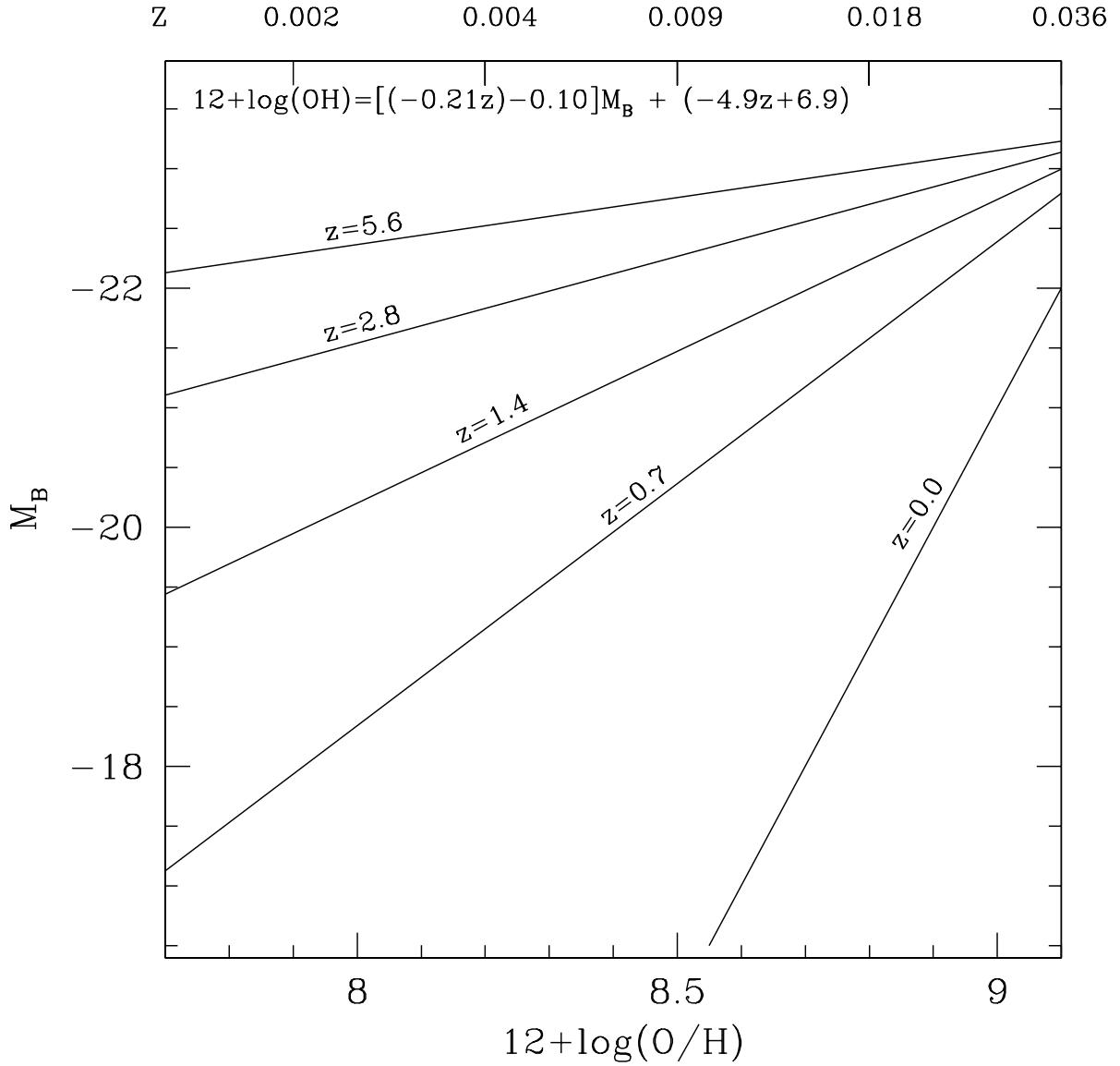


Fig. 13.— Hypothetical L-Z relation as a function of redshift based upon the data in Figure 12. Data at  $z=0.7$  are the most distant reliable data, and the  $z=3$  galaxies are highly uncertain, so this relation should not be blindly extrapolated to high redshifts or extremely low luminosities. The evolution of the L-Z relation with cosmic epoch is plausibly due to a longer gas accretion timescale and lower star formation rates for the lower mass galaxies. An analytical expression approximating the evolution of the L-Z relation is given in the figure.

Table 1. DGSS Selected Galaxies

ID	Object	RA (2000)	DEC (2000)	z	$I_{814AB}$	$M_B$	$(B-V)$	$R_{hl}$	$B/T$	$R_T$	$R_A$	$EW_{3727}$	$EW_{4861}$	$EW_{4959}$	$EW_{5007}$	$12 + \log(O/H)$	$SFR$	Notes
(1)	(2)	(3)	(4)	(5)	(6)	(7)	(8)	(9)	(10)	(11)	(12)	(13)	(14)	(15)	(16)	(17)	(18)	(19)
1	072-2273	14:17:38.928	52:29:34.72	0.2888	22.03	-18.0	0.36	2.36	0.00	0.03	0.05	49.5±1.4	10.1±0.4	6.5±0.4	25.7±0.4	8.52±0.03	0.3	A
2	072-4040	14:17:37.838	52:28:58.44	0.2908	20.01	-19.6	0.70	9.42	0.00	0.15	0.06	26.9±1.1	5.9±0.3	1.7±0.2	5.7±0.2	8.71±0.03	1.0	A
3	172-1242	14:16:35.570	52:17:27.91	0.3288	24.22	-16.4	0.44	1.37	0.10	-0.02	0.01	22.9±1.7	30.2±3.6	39.1±3.9	121±4	8.73±0.04	0.1	A,B
4	092-1375	14:17:26.699	52:27:19.48	0.3315	23.84	-16.6	0.39	1.54	0.15	0.06	0.04	22.8±1.2	12.6±0.7	13.2±0.7	32.5±0.7	8.75±0.02	0.1	A,B
5	134-2322	14:17:05.547	52:21:18.17	0.3319	21.28	-18.3	1.02	2.39	0.34	0.05	0.15	39.1±1.0	9.9±0.5	10.8±0.6	24.1±0.5	8.58±0.03	0.7	A
6	142-4644	14:16:51.341	52:20:52.38	0.3322	21.52	-18.8	0.47	3.62	0.00	0.03	0.01	76.1±1.2	19.2±1.6	6.9±1.9	30.5±2.1	8.63±0.07	1.2	A
7	223-2132	14:16:07.432	52:11:25.04	0.3359	23.16	-17.2	0.48	1.16	0.04	-0.01	0.00	33.8±2.8	6.8±0.9	5.1±0.8	15.1±1.1	8.57±0.10	0.1	A
8	124-3864	14:17:14.790	52:21:50.38	0.3564	21.55	-18.8	0.56	3.02	0.00	0.05	0.07	34.2±3.3	7.2±0.5	0.8±0.7	2.5±0.5	8.71±0.07	0.5	A
9	103-6061	14:17:27.434	52:26:08.93	0.3631	21.88	-18.6	0.51	0.93	0.49	0.03	0.01	38.9±0.7	10.9±0.6	4.4±0.5	11.3±0.5	8.74±0.03	0.6	A
10	203-4851	14:16:21.680	52:14:14.78	0.3639	22.58	-18.1	0.36	1.18	0.70	0.02	0.01	52.6±1.1	12.2±0.4	13.8±0.4	34.6±0.4	8.42±0.02	0.3	A
11	313-3557	14:15:11.917	52:01:10.88	0.3757	20.56	-20.2	0.42	2.35	0.25	0.06	0.04	44.4±0.9	13.3±0.2	3.3±0.1	9.0±0.2	8.78±0.01	2.8	A
12	304-4028	14:15:17.787	52:01:23.63	0.3760	22.78	-17.9	0.41	1.38	0.02	0.03	0.04	99.5±1.1	27.8±1.3	14.6±1.6	46±1.6	8.64±0.02	0.7	A
13	193-5319	14:16:24.702	52:15:23.83	0.3929	20.62	-20.1	0.46	4.45	0.03	0.06	0.07	55.5±0.4	12.5±0.2	2.3±0.2	7.3±0.4	8.69±0.01	2.8	A
14	304-3354	14:15:17.610	52:00:56.86	0.4263	20.57	-20.6	0.29	1.90	0.51	0.09	0.12	113±2	44.3±2.4	30.0±2.6	97.1±2.6	8.68±0.02	12.7	A
15	223-6341	14:16:07.359	52:12:07.83	0.4263	21.94	-19.2	0.29	2.71	0.06	0.06	0.07	82.1±2.2	19±2.2	14.4±1.1	48.1±1.1	8.52±0.07	1.5	A
16	292-3870	14:15:14.882	52:03:47.19	0.4266	20.90	-20.2	0.36	2.98	0.00	0.19	0.08	63.6±2.2	19.9±2.2	11.9±1.1	40.0±1.1	8.66±0.05	4.2	A
17	093-6667	14:17:34.454	52:27:25.05	0.4306	23.08	-18.0	0.34	3.07	0.01	-0.00	0.01	39.5±0.9	17.1±0.5	28.2±0.5	57.1±0.5	8.61±0.01	0.5	A
18	164-3515	14:16:47.287	52:17:57.62	0.4320	21.74	-19.3	0.42	3.23	0.01	0.02	0.02	54.8±0.8	12.2±1.1	3.2±1.3	14.3±1.3	8.64±0.05	1.2	A
19	164-2417	14:16:46.114	52:17:53.61	0.4323	21.30	-19.8	0.38	3.86	0.08	0.08	0.08	78.4±0.8	16.2±1.7	8.5±2.0	29.2±2.0	8.53±0.07	2.4	A
20	074-4757	14:17:48.165	52:27:48.29	0.4323	21.49	-19.6	0.40	4.82	0.03	0.15	0.09	103±2	24.7±1.5	11.6±1.3	38.8±1.5	8.60±0.03	3.1	A
21	094-1054	14:17:31.025	52:25:24.32	0.4331	19.66	-21.3	0.54	5.37	0.10	0.09	0.11	11.5±0.6	4.2±0.2	0.6±0.4	2.0±0.2	8.93±0.03	2.8	A
22	183-4770	14:16:36.632	52:16:38.91	0.4691	21.38	-19.9	0.41	1.85	0.56	0.05	0.06	121±1	45.1±3.0	53.7±3.2	126±3	8.60±0.03	7.7	A
23	223-7714	14:16:04.136	52:12:15.01	0.4711	21.72	-19.4	0.53	2.12	0.31	0.02	0.04	32±1.3	7.8±0.2	2±0.2	6.0±0.3	8.73±0.02	0.9	A
24	062-1570	14:17:46.321	52:30:43.30	0.4770	21.38	-19.9	0.45	2.49	0.34	0.05	0.06	26.9±0.6	6.9±0.4	4.6±0.4	15.9±0.4	8.65±0.03	1.2	A
25	162-5547	14:16:37.359	52:18:33.42	0.4776	21.24	-20.0	0.48	2.03	0.03	0.06	0.05	73.2±0.8	22.1±0.6	7.3±0.6	24.5±0.6	8.73±0.01	4.5	A
26	083-6536	14:17:37.724	52:28:28.13	0.4798	23.75	-17.6	0.45	0.44	0.26	0.03	-0.02	55.5±1.7	14.2±1.2	13.6±1.3	38.9±1.7	8.55±0.05	0.2	A
27	212-2260	14:16:08.191	52:13:03.10	0.4832	21.43	-19.9	0.42	2.77	0.14	0.08	0.08	94.1±0.6	22.7±0.2	11.7±0.2	38.9±0.2	8.59±0.01	3.9	A
28	303-1256	14:15:18.750	52:01:58.57	0.4850	22.09	-19.3	0.41	5.05	0.52	0.05	0.08	98.5±4.3	30.9±2.5	16.8±2.8	65.3±2.8	8.64±0.04	3.0	A
29	303-3546	14:15:17.146	52:02:18.14	0.4850	20.52	-20.7	0.51	4.96	0.10	0.04	0.06	41.6±0.4	11.2±0.4	1.6±0.5	5.1±0.5	8.77±0.02	4.6	A
30	262-5149	14:15:33.122	52:06:56.39	0.5084	23.14	-18.3	0.46	2.64	0.08	0.02	-0.03	70.6±1.0	21.0±2.3	25.5±1.9	92±1.9	8.47±0.06	0.8	A
31	114-3114	14:17:19.113	52:23:47.26	0.5470	21.59	-20.1	0.46	3.43	0.03	0.03	0.04	78.8±2.0	15.3±1.0	3.1±1.0	6.1±1.0	8.60±0.04	3.1	A
32	283-3961	14:15:31.425	52:04:46.65	0.5586	23.57	-18.1	0.51	1.07	0.63	0.04	0.03	134±2.2	52.3±8.6	71.2±10.4	239±11	8.49±0.09	1.8	A
33	082-1064	14:17:33.800	52:28:19.15	0.6039	23.26	-18.7	0.41	1.36	0.18	-0.01	0.06	40.6±0.6	8.2±0.8	5.5±0.8	21.1±0.8	8.53±0.07	0.4	A
34	282-2474	14:15:22.654	52:05:04.57	0.6315	21.52	-20.6	0.46	2.35	0.30	0.03	0.05	38.2±0.7	12.2±0.6	4.7±0.3	10.9±0.3	8.78±0.02	3.6	A
35	282-3252	14:15:22.320	52:04:41.62	0.6317	22.33	-19.8	0.34	3.09	0.01	0.08	0.07	118±1	36.2±0.9	50.1±0.5	141±2	8.47±0.01	4.7	A
36	212-6648	14:16:03.907	52:12:41.35	0.6371	23.66	-18.5	0.36	1.92	0.02	0.05	0.09	117±2	75.1±9.7	152±4	560±10	8.50±0.07	3.1	A

Table 1—Continued

ID	Object	RA (2000)	DEC (2000)	z	$I_{814}AB$	$M_B$	$(B - V)$	$R_{hl}$	$B/T$	$R_T$	$R_A$	$EW_{3727}$	$EW_{4861}$	$EW_{4959}$	$EW_{5007}$	$12 + \log(O/H)$	$SFR$	Notes
(1)	(2)	(3)	(4)	(5)	(6)	(7)	(8)	(9)	(10)	(11)	(12)	(13)	(14)	(15)	(16)	(17)	(18)	(19)
37	093-6526	14:17:30.101	52:27:15.58	0.6431	23.45	-18.7	0.38	1.67	0.37	0.01	0.04	63.1±0.4	15.3±1.5	15.8±0.6	50.3±0.6	8.49±0.06	0.7	A
38	063-5323	14:17:49.728	52:30:31.88	0.6437	21.27	-20.9	0.32	4.29	0.00	0.19	0.14	57.0±0.2	19.8±0.3	10.8±0.3	34.1±0.3	8.72±0.01	7.1	A
39	262-3751	14:15:34.530	52:07:00.73	0.6497	20.74	-21.3	0.50	4.68	0.10	0.18	0.14	17.4±1.5	5.2±0.5	0.5±0.4	4.1±0.4	8.85±0.06	3.7	A
40	284-3046	14:15:30.071	52:03:24.75	0.6506	23.35	-18.8	0.46	1.08	0.77	0.00	0.02	79.3±1.9	19.8±1.9	23.6±2.9	61.4±2.9	8.49±0.06	1.1	A
41	172-5435	14:16:31.329	52:17:11.67	0.6605	22.55	-19.6	0.48	3.61	0.01	0.08	0.03	49.1±0.9	10.3±0.9	4.4±2.1	11.8±1.9	8.62±0.06	1.3	A
42	152-1633	14:16:48.315	52:19:38.62	0.6736	21.80	-20.5	0.44	6.99	0.02	0.06	0.09	119±2	27.0±0.9	14.3±5.7	44±5.7	8.56±0.03	7.2	A
43	063-7209	14:17:47.868	52:30:47.38	0.6760	21.01	-21.3	0.33	3.73	0.49	0.09	0.17	69.3±0.3	34.1±0.3	16.1±0.9	50.8±1.7	8.80±0.01	17.2	A
44	164-3859	14:16:48.501	52:17:15.55	0.6828	22.42	-19.9	0.47	4.62	0.02	0.03	0.05	64.1±1.9	14.5±1.1	3.9±1.9	11.5±1.9	8.65±0.05	2.3	A
45	292-4369	14:15:14.367	52:03:45.35	0.6926	20.61	-21.7	0.47	3.41	0.58	0.07	0.09	39.3±0.5	22.2±1.7	11.5±3.7	34.6±3.7	8.83±0.03	19.6	A
46	282-6050	14:15:19.468	52:04:32.81	0.6946	22.70	-19.7	0.39	2.50	0.01	0.08	0.12	97.9±1.8	35.4±1.8	29.4±2.8	103±3.0	8.61±0.03	4.3	A
47	153-3721	14:16:51.198	52:19:47.44	0.7043	21.07	-21.4	0.32	3.19	0.25	0.10	0.08	71.5±0.9	32.0±0.9	23.4±0.9	71±0.9	8.72±0.01	16.9	A
48	292-7343	14:15:11.836	52:03:14.00	0.7450	23.56	-19.0	0.29	1.64	0.02	0.03	0.07	99.1±1.8	24.1±4.4	26.3±4.5	79.6±3.6	8.46±0.12	1.4	A
49	084-6809	14:17:42.554	52:27:29.20	0.7467	21.92	-20.6	0.46	6.54	0.09	0.10	0.12	121±2	26.2±1.8	16.0±2.0	48±2.0	8.52±0.04	8.0	A
50	182-7536	14:16:22.681	52:15:59.33	0.7505	22.73	-19.8	0.40	3.86	0.04	0.07	0.08	72.5±1.8	18.2±1.2	13.7±1.4	37.9±1.4	8.57±0.04	2.4	A
51	292-6724	14:15:12.920	52:02:56.62	0.7659	21.93	-20.7	0.47	3.37	0.09	0.06	0.10	35.3±0.9	11.3±0.9	4.2±1.6	11.8±1.6	8.77±0.04	3.7	A
52	134-0967	14:17:05.035	52:20:31.42	0.7885	22.83	-19.9	0.26	3.76	0.00	0.14	0.07	117±2	51.9±1.9	58.1±2.5	225±3	8.55±0.02	6.9	A
53	142-4838	14:16:51.266	52:20:45.96	0.8077	20.18	-22.6	0.28	5.17	0.25	0.16	0.09	13.1±1.9	11.4±0.5	9.5±0.7	33.3±0.5	8.80±0.02	18.5	A
54	174-3527	14:16:40.994	52:16:35.72	0.8096	21.59	-21.2	0.46	3.19	0.00	0.10	0.18	56.9±1.7	25.8±3.1	10.4±2.1	23.9±2.1	8.84±0.04	13.2	A
55	152-3226	14:16:46.841	52:19:28.70	0.8127	22.52	-20.3	0.34	4.42	0.42	0.05	0.10	109±2	28.3±4.4	22.9±3.0	88.8±3.0	8.50±0.09	5.4	A
56	153-6078	14:16:56.673	52:20:22.44	0.8128	20.98	-21.8	0.48	6.87	0.06	0.14	0.15	70.0±5.2	59.5±7.9	7.7±1.5	23.4±1.5	9.00±0.02	58.3	A
57	073-2658	14:17:47.597	52:29:03.36	0.2863	21.13	-18.9	0.34	2.88	0.28	0.04	0.10	62.1±1.6	10.8±1.1	11.1±2.2	23.0±1.2	8.44±0.07	0.7	C
58	173-5210	14:16:36.664	52:17:39.89	0.3570	20.03	-20.4	0.54	4.51	0.05	0.07	0.06	36.9±0.9	5.8±0.4	1.4±0.4	3.5±0.4	8.58±0.05	1.7	C
59	213-6640	14:16:13.664	52:13:20.44	0.3656	20.22	-20.3	0.50	4.62	0.03	0.06	0.05	29.2±1.4	3.5±0.3	0.5±0.3	0.8±0.3	8.51±0.10	0.9	C
60	183-6415	14:16:30.453	52:16:42.93	0.3865	21.00	-19.6	0.55	7.06	0.00	0.14	0.07	131±4	24.2±2.5	8.3±2.5	27.8±2.7	8.51±0.07	3.6	C
61	092-1962	14:17:26.421	52:27:06.04	0.4261	19.49	-21.5	0.40	6.35	0.03	0.20	0.15	25.7±0.2	4.3±0.2	1.0±0.1	4.3±0.1	8.64±0.03	3.3	C
62	313-7545	14:15:09.713	52:01:46.44	0.4503	22.70	-18.4	0.42	2.54	0.01	0.01	0.01	54.9±12.1	9.1±0.8	6.8±1.1	24.6±1.1	8.42±0.14	0.4	C
63	183-1153	14:16:35.713	52:16:00.42	0.5070	20.74	-20.8	0.39	5.96	0.42	0.09	0.13	64.3±2.1	10.6±0.6	3.6±0.6	15.5±0.6	8.48±0.05	3.9	C
64	293-4412	14:15:19.779	52:03:30.50	0.6462	22.90	-19.3	0.30	6.21	0.00	0.04	0.05	175±2	32.8±2.1	20.2±1.9	96.5±1.9	8.38±0.04	2.8	C
65	092-7832	14:17:20.880	52:26:23.36	0.6824	23.57	-18.7	0.29	1.43	0.54	0.00	0.10	59.0±1.9	154±0.7	117±4	237±4	8.93±0.04	8.2	D
66	203-3109	14:16:17.618	52:13:49.43	0.6848	22.41	-19.9	0.34	5.60	0.02	0.10	0.08	60.5±1.7	30.2±1.5	11.3±2.2	31.1±2.2	8.85±0.02	4.9	D

References. — (1) Reference ID # for this paper; (2) Groth Strip survey ID ; (3) J2000 Right Ascension; (4) J2000 Declination; (5) redshift from optical emission lines (6)  $I_{814}$  AB magnitude (7) Rest-frame  $M_B$  for  $H_0 = 70$  km/s/Mpc,  $\Omega_M = 0.3$ ,  $\Omega_\Lambda = 0.7$  (8) Rest-frame B-V color (9) Half light radius in kpc derived from the global  $I_{814}$  image (10) Bulge fraction derived from the  $I_{814}$  image. (11)  $R_T$  asymmetry index as defined in paper II (12)  $R_A$  asymmetry index as defined in Paper II (13) EW of [O II]  $\lambda 3727$  and uncertainty corrected to the rest frame (14) EW of  $H\beta$   $\lambda 4861$  and uncertainty corrected to the rest frame (15) EW of [O III]  $\lambda 4959$  and uncertainty corrected to the rest frame (16) EW of [O II]  $\lambda 5007$  and uncertainty corrected to the rest frame (17) Oxygen abundance,  $12+\log(O/H)$ , from the empirical  $R_{23}$  method following McGaugh (1991) as formulated in KKP after correction for  $\dot{A}$  of stellar absorption in the  $EW_{H\beta}$ . An additional uncertainty of  $\sim 0.15$  dex in  $O/H$  representing uncertainties in the photoionization models and empirical strong-line calibration should be added in quadrature to the tabulated measurement errors. ; (18) Estimated star formation rate based on  $H\beta$  flux (not corrected for stellar absorption), derived from the  $EW(H\beta)$  and V-band absolute magnitude. We estimate the  $H\beta$  luminosity as  $L_{H\beta}(erg/s) = 5.49 \times 10^{31} \times 2.5^{-M_V} \times EW_{H\beta}$ . The SFR then is then computed by  $SFR(M_\odot/yr) = 2.8 \times L_{H\beta}/1.12 \times 10^{41}$  which assumes the Kennicutt (1983) calibration of SFR in terms of  $H\alpha$  luminosity. This estimate is a lower limit since extinction and stellar Balmer absorption is not taken into account here. (19) Notes: A—Probable star-forming galaxy (non-AGN or minimal AGN contribution), as defined in text; B—Low-luminosity object with line ratios in the “turn-around” region of the strong-line abundance diagram, so the oxygen abundance is highly uncertain, in the range  $7.8 < 12 + \log(O/H) < 8.4$ . Object removed from remaining analysis. C—Object is probable AGN on basis of Figure 3; D—Object is a probable AGN on basis of  $[Ne\ III]/[O\ II] > 0.4$